Frequency Doubling and Spectroscopy using Fiber Amplifiers

Abul Lais

Department of Physics

A Thesis submitted to the Department of Physics, National University of Singapore, in partial fulfillment of the requirements for the degree of

Bachelor of Science (Honors) in Physics

6 April 2014

Keywords: Nonlinear Optics, Second Harmonic Generation, Frequency Doubling, Quasi-Phase Matching, Periodically-Poled Lithium Niobate

Abstract

We have developed a 780.24 nm laser source for Rubidium cooling by frequency doubling the fiber-amplified output (20 W maximum) of a 1560 nm distributed feedback semiconductor seed laser. The doubling is performed using a periodically-poled lithium niobate nonlinear crystal, through a process called quasi-phase matching. We want to maximize the conversion efficiency of the seed laser frequency (1560 nm) into its second harmonic (780 nm), for which we have investigated the following factors: input power and polarization, temperature and poling period, and position of focal point. Their influences on the conversion efficiency are measured and presented graphically. After optimizing these factors, we have measured the temporal behavior of the power and wavelength of the frequency-doubled beam, and have graphically presented these as well. Next, we review a few factors whose influence on conversion efficiency went unresearched for want of time, and these set a signpost for future research efforts. We conclude by studying safety issues pertaining to high-power laser beams, and look at ways to estimate if the optics used are compatible with the laser and amplifier utilised.

Acknowledgements

I wish to thank members of the Cold Atom Laboratory (Dr Bjorn's Hessmo's group) for all the assistance they have rendered in the completion of this project. In addition, gratitude is extended to the Rydberg Atom Laboratory (Dr Li Wenhui's group) for the loan of equipment which was instrumental in the completion of this project.

Contents

List of tables

List of Acronyms and Abbreviations

CW	continuous wave (laser)
FWHM	full-width at half maximum
PBS	polarizing beamsplitter
PPLN	periodically-poled lithium niobate
QPM	quasi-phase matching
HWP/QWP	half-wave/quarter-wave plate
SHG	second harmonic generation

1. Rationale for project

Laser cooling and manipulation of rubidium atoms requires several hundreds of milliwatts of light at 780 nm. The telecommunications industry has focused on developing the 1500 – 1600 nm wavelength band because silica glass – used in fiber optics for long-haul communications – attains an attenuation loss minimum near 1550 nm. Consequently, it is quite difficult to source out reliable high-power diodes, optical amplifiers and phase modulators operating near 780 nm, with which Rubidium laser-cooling can be performed. The latest generation of Ti:sapphire lasers offers high power output and better reliability than previously available, but it is relatively expensive. The entire system, including pump laser and fluid cooling loop, is not very compact [1] and requires regular alignment and maintenance. Hence, it is desirable to develop a compact, rugged laser set-up for rubidium cooling that uses easily available components. Fortunately, the telecommunications spectrum of 1500 – 1600 nm is just double of the wavelength that laser cooling of rubidium demands (the rubidium D2 transition line – to be exploited in laser cooling – is at 780.24 nm). Frequency doubling a telecom laser is a suitable laser source for rubidium cooling, whilst the vast array of resources developed for the telecom industry is simultaneously opened up to atomic physicists working with rubidium.

2. Overview of project

We have developed a source of 780 nm laser light by frequency doubling the amplified output of a 1560 nm telecom laser. The seed laser is a fiber-coupled, distributed-feedback (DFB) semiconductor laser that is tunable within the 1559 – 1561 nm bandwidth. The DFB laser has a linewidth of 100 kHz, is intrinsically single-mode, and generates outputs of 1 – 5 mW. This is fed into an erbium-doped fiber amplifier which boosts the laser output to 20 W, which is then frequency doubled using a periodically poled lithium niobate (PPLN) nonlinear optical crystal.

3. Introduction to Nonlinear optics

The frequency doubling process (or second harmonic generation) mentioned previously is the most prominent example of nonlinear optics, which is a class of light-matter interactions wherein the optical properties of a medium are modified by light. Typically, one thinks of linear optics in the following fashion: light enters a medium, gets modified by the latter before exiting it. The modification induced is an intrinsic property of the medium independent of the incident light.

In contrast, for nonlinear optics, the modification induced is itself dependent on the incident light. Besides SHG, another nonlinear optical phenomenon is the intensity-dependence of the refractive index; it occurs when a highly-intense light beam strikes a suitable nonlinear optical crystal, which changes the refractive index of the medium, thereby further refracting the light. Hence, the modification induced in the optical path taken by the incident light depends on both the medium of propagation and the strong intensity of the incident light. Usually, only laser beams possess sufficient intensity to modify the properties of matter.

The "nonlinearity" in nonlinear optics refers to the response (output) being nonlinear as a function of the driving force (input). A mechanical analogue is a spring with two balls attached to either end, wherein the Hooke's law regime dictates that the extension (output) of the spring is directly proportional to the agent exerting a force on the spring (input). Beyond a certain threshold extension, the extension of the spring fails to respond linearly to the driving force, and the Hooke's law regime is breached. This can be translated directly into the optical realm by replacing the balls and springs with atoms and electronic bonds, and the driving force by a propagating electromagnetic wave. So, how exactly does this process convert a 1560 nm infrared beam passing into a nonlinear crystal into a 780 nm output beam?

To understand this, we consider a simple model which illustrates the process of nonlinear frequency conversion at the atomic scale. Suppose the nonlinear crystal is composed of atoms comprising a positively charged nucleus surrounded by an electron cloud. In equilibrium, the positive and negative charge centers coincide, so the net polarization of the material vanishes (Figure 1(a)). If a light wave with frequency ω_1 strikes the material, the associated electric field

exerts a force on the electron cloud and distorts it; this distortion physically separates the positive and negative charge centers which induces an electric polarization within the material (Figure 1(b)).

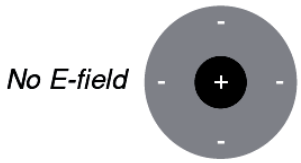

Figure 1(a)

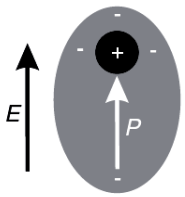

Figure 1(b)

Figure 1 [2]: The black center represents the positively charged nucleus whilst the outer gray ring represents the surrounding electron cloud.

(a) When no electric field is present, the centers of positive and negative charge coincide and there is no induced polarization.

(b) An applied electric field distorts the electron cloud so that the centers of charge are spatially separated and an electric polarization is induced.

Whilst the electron cloud is being driven by the time-varying electric field of the incident light – from one side of the nucleus to the other – an oscillating polarization is simultaneously created. If there exists a linear relationship between the polarization and applied electric field, the time-varying polarization is also sinusoidal at frequency ω_1. Since an accelerating charge radiates an electromagnetic wave, this sinusoidally-varying polarization radiates its own electric field at frequency ω_1, just like an antenna wire. The electric field radiated by the polarization interferes with the electric field originally present in the material, and this interference leads to the phase shift which is attributed to the refractive index of the material.

In contrast, if the relationship between the induced polarization P and the electric field E is nonlinear (i.e. the Polarization v Electric Field curve is not a straight line), the generated polarization is not equivalent for an applied field whose strength is $+E_0$ as it is for a field of $-E_0$. This point is illustrated In Figure 2 (top left graph) by considering that the polarization P_2 is much greater in magnitude than P_1. Consequently, the polarization response to an applied sinusoidal field (Figure 2, bottom left) is not a pure sinusoid, but is distorted (Figure 2, top right, dark

curve). This distortion signals the presence of components in the polarization response at frequencies other than ω_1, such as the strong second-harmonic frequency component at $2\omega_1$ (Figure 2, top right, light line in lower half). This is the atomic origin of SHG.

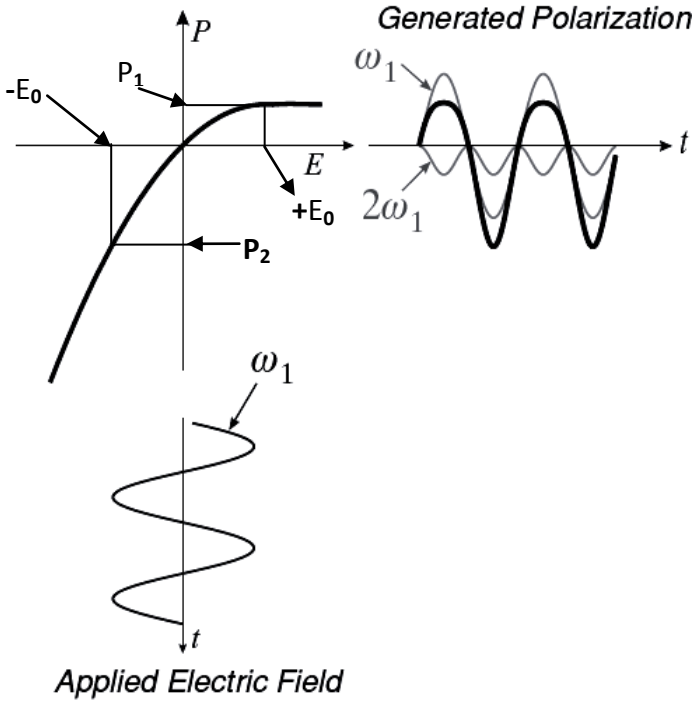

Figure 2 [2]: For a nonlinear medium, where the polarization is related to the applied electric field in a nonlinear way, a sinusoidally-varying electric field will induce a polarization that contains frequency components at higher harmonics of the incident frequency. In this example (top right graph), the induced polarization response (dark black curve) can be decomposed into a component at the applied frequency and at the second harmonic of the applied frequency (light gray trace).

We can mathematically describe the complete relationship between the polarization P(t) and the applied electric field E(t) depicted in Figure 2 by means of a power series expansion:

$$\boldsymbol{P^{nonlinear}(t) = \epsilon_0\left[\chi^{(1)}E(t) + \chi^{(2)}E(t)^2 + \chi^{(3)}E(t)^3 + \cdots\right] - - - (1)}$$

The $\epsilon_0\chi^{(1)}E$ term is called the first-order (linear) polarization whereas the $\epsilon_0\chi^{(2)}E^2$ and $\epsilon_0\chi^{(3)}E^3$ terms are, respectively, known as the second- and third-order nonlinear polarizations. The different orders correspond to different oscillation modes of the time-varying polarization. Different phenomena occur depending on the order of the polarization. The first term of this

expansion causes first-order (or linear) phenomena, such as the refraction of light. The second-order term, involving the square of the electric field, gives rise to second-order nonlinear effects such as second harmonic generation (SHG), sum-frequency generation and optical rectification. The third-order term, involving the cube of the electric field, gives rise to effects such as third-harmonic generation, intensity-dependent refractive index, and Brillouin scattering. Some of these processes are summarized in the table hereunder:

Second-order Nonlinear Polarization	**Third-order Nonlinear Polarization**
Second Harmonic Generation **ω(out) = 2 x ω(in)**	Third Harmonic Generation **ω(out) = 3 x ω(in)**
Sum Frequency Generation **ω(out) = ω_1(in) + ω_2(in)**	Intensity-dependent refractive index
Difference Frequency Generation **ω(out) = ω_1(in) - ω_2(in)**	
Optical Rectification **A static electric field is generated within the crystal.**	

Table 1: A list of the various optical processes that can occur as a result of the second-order (left column) and third-order (right column) nonlinear polarization discussed in the preceding paragraph.

For this paper, we shall restrict attention to the nonlinear second-order $\chi^{(2)}$ term, which is directly related to SHG, in which a single laser beam of frequency ω_1 is passed through a nonlinear crystal and frequency-doubled light emerges with frequency $2\omega_1$. This current research was conducted in the Cold Atom Laboratory, where an intense laser beam at 780 nm is needed for spectroscopy and trapping of Rubidium atoms, so the incident beam was pumped using a 1560 nm distributed feedback semiconductor laser source. Figure 3 is an overview of the SHG process.

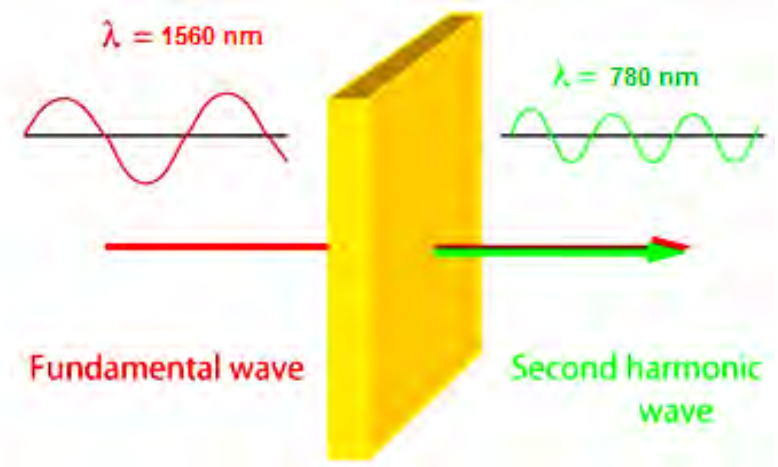

Figure 3: A graphic representation of the second harmonic generation (SHG) process, also known as frequency doubling, in which the "colour" (or frequency) of an incident light is being altered.

In Figure 2, we looked at SHG through a graphical approach, which signaled the presence of new frequency components in the output that were absent in the input light. This approach is qualitative, at best. Equation (1) offers the prospect of proving rigorously the presence of the second-harmonic. Suppose – to a nonlinear crystal – we apply a monochromatic light wave field of the typical form:

$$\mathbf{E} = \widetilde{\mathbf{E_0}}\mathbf{e^{-i\omega t}}$$

In this case,

$$\mathrm{P^{nonlinear}} = \varepsilon_0 \left[\ldots + \chi^{(2)} (\mathrm{E_o})^2 \left(\mathrm{e^{-i\omega t}}\right)^2 + \ldots \right]$$

$$= \left[\ldots + \varepsilon_0 \chi^{(2)} (\mathrm{E_o})^2 \, \mathrm{e^{-i(2\omega t)}} + \ldots \right]$$

The output contains a 2ω component even if only ω was input – the frequency has been doubled! The aforementioned procedure is formally known as the time-domain approach to nonlinear optics, as the electric field and polarization are expressed as functions of time. This perspective works for simple monochromatic input fields, but becomes cumbersome when

more complicated mixed-frequency fields are involved. In that case it is perhaps more natural to use a frequency-domain description, which is related to the time-domain description through the Fourier transform. Since our incident laser is an ultra-low linewidth DFB laser, which typically oscillates in a single longitudinal mode, we shall not venture into the frequency domain approach.

For the SHG process to occur, the standard conservation laws must be applied. Conservation of energy is guaranteed by Planck's relation. Since we are annihilating 2 photons at ω_1 and generating one photon at $\omega_2 = 2\omega_1$, conservation of energy is satisfied.

Conservation of momentum must also be taken into account, since the interacting particles (photons) are all momentum carriers. In nonlinear optics, it is more convenient to refer to wavevector conservation than momentum conservation. The relation $p = \hbar k$ connects the momentum (p) to the wavevector (k). The subscripts 1 and 2 refer to the incident fundamental and second harmonic output beams respectively. By conservation of momentum, we have:

$$2p_1 = p_2$$

using $p = \hbar k$, we arrive at

$$2\hbar k_1 = \hbar k_2$$

and after simplifying, we get

$$2k_1 = k_2$$

which leads us to the equation formally known as the phasematching condition

$$2k_1 - k_2 = \Delta k = 0 - - - (2)$$

This is the defining equation of SHG. Its fulfillment directly impacts the efficiency of the SHG process, i.e. the conversion of the incident fundamental beam to its second harmonic. The goal of SHG is not simply to double some photons at fundamental frequency; rather it is to convert as much of the fundamental power into its second harmonic as is possible. Conservation of energy is guaranteed by using photons at half the desired frequency, so the entire business of SHG (or frequency doubling) boils down to meeting the phasematching condition. What happens if the phasematching criterion is not satisfied? Equation (1) implies that there will possibly be several harmonics generated in any nonlinear interaction. We would like to suppress the extra

components and magnify the second harmonic one by fulfilling its requisites. Typically, the different harmonics necessitate different conditions; this is clear from the condition for SHG i.e. $2k_1 - k_2 = 0$. The factor of two arises from the frequency doubling process, and for third harmonic generation, the condition would be: $3k_1 - k_2 = 0$. Hence, if the set-up is tuned with such parameters that only the phasematching conditions for SHG are satisfied, we are able to maximize the amount of second harmonic photons that are generated. Hence, the whole SHG task reduces to one of finding the right conditions for it. In this paper, we will be investigating the various physical factors that can be varied to study how they affect the SHG efficiency factor (which we define as the power generated at the second harmonic per unit power input at fundamental frequency). Returning to equation (2), we can simplify it by substituting $k = 2n\pi/\lambda$

$$2\frac{2n_1\pi}{\lambda_1} - \frac{2n_2\pi}{\lambda_2} = 0$$

and exploiting the relation $2\lambda_2 = \lambda_1$, we obtain

$$2\frac{2n_1\pi}{2\lambda_2} - \frac{2n_2\pi}{\lambda_2} = 0$$

which yields

$$\therefore n_1 = n_2 - - - (3)$$

Hence, in the specific case of SHG, the phasematching condition simply means that both the fundamental frequency and second harmonic must encounter the same refractive index. Even though both beams are travelling in the same medium, this condition is quite challenging to fulfill as chromatic dispersion implies that the refractive index is a monotonically-decreasing function of wavelength, as evidenced by Figure 4 [3].

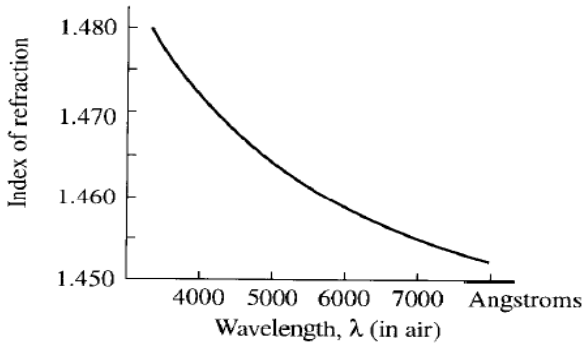

Figure 4: Due to material dispersion, the refractive index of light propagating in a medium is uniquely dependent on the wavelength of the light.

The beam at the fundamental and second harmonic would definitely experience different refractive indices, unless some extraneous factor helps overcome the refractive index difference arising from chromatic dispersion.

Two such factors have been commonly utilized by nonlinear optics workers:

(a) birefringent phase matching
(b) quasi-phase matching

For birefringent phasematching, the goal is to satisfy the condition $n_1 = n_2$ (equation (3)) or, equivalently, $\Delta k = 0$ (equation (2)), as closely as possible. Briefly speaking, a birefringent crystal is an optical material in which the refractive index depends on the polarization of the wave. This property can be used to compensate the refractive index difference between the fundamental and second-harmonic wave resulting from normal dispersion by arranging the fundamental and second harmonic beams to have different polarizations.

However, this approach is subject to certain limitations, as stated by Boyd [4]:

(i) certain crystals lack birefringence entirely, or

(ii) the birefringence present may not be sufficient to compensate the effects of chromatic dispersion; this severity of this issue increases at higher frequencies as the refractive index rises rapidly at higher frequencies but the birefringence (difference between the ordinary and extraordinary refractive indices) tends to be more nearly constant.

In this paper, we will be utilizing the second approach known as quasi-phase matching (QPM), which generates second harmonic output without actually fulfilling the phasematching condition $\Delta k = 0$.

We first lay the visual framework upon which the theory shall be laid. The graph in Figure 5 [5] encapsulates the entire theory of SHG and phasematching. The vertical axis represents the intensity of the second harmonic light generated (the chief quantity of interest) as a function of the crystal length. Graph A exemplifies perfect birefringent phasematching ($\Delta k = 0$), Graph B portrays imperfect birefringent phasematching ($\Delta k \neq 0$), whilst Graph C represents quasi-phasematching ($\Delta k \neq 0$ but with corrective mechanism).

In addition, we introduce the concept of a coherence length l_c as the maximum distance over traversed over which the second harmonic waves generated are in phase with each other. This implies that the second harmonic intensity is expected to rise in magnitude for a distance of up to one coherence length, before the second harmonic waves begin slipping out of phase and some power is re-converted back to fundamental frequency, which causes the second harmonic intensity to drop. The distance equivalent to one l_c will be evaluated in equation (6).

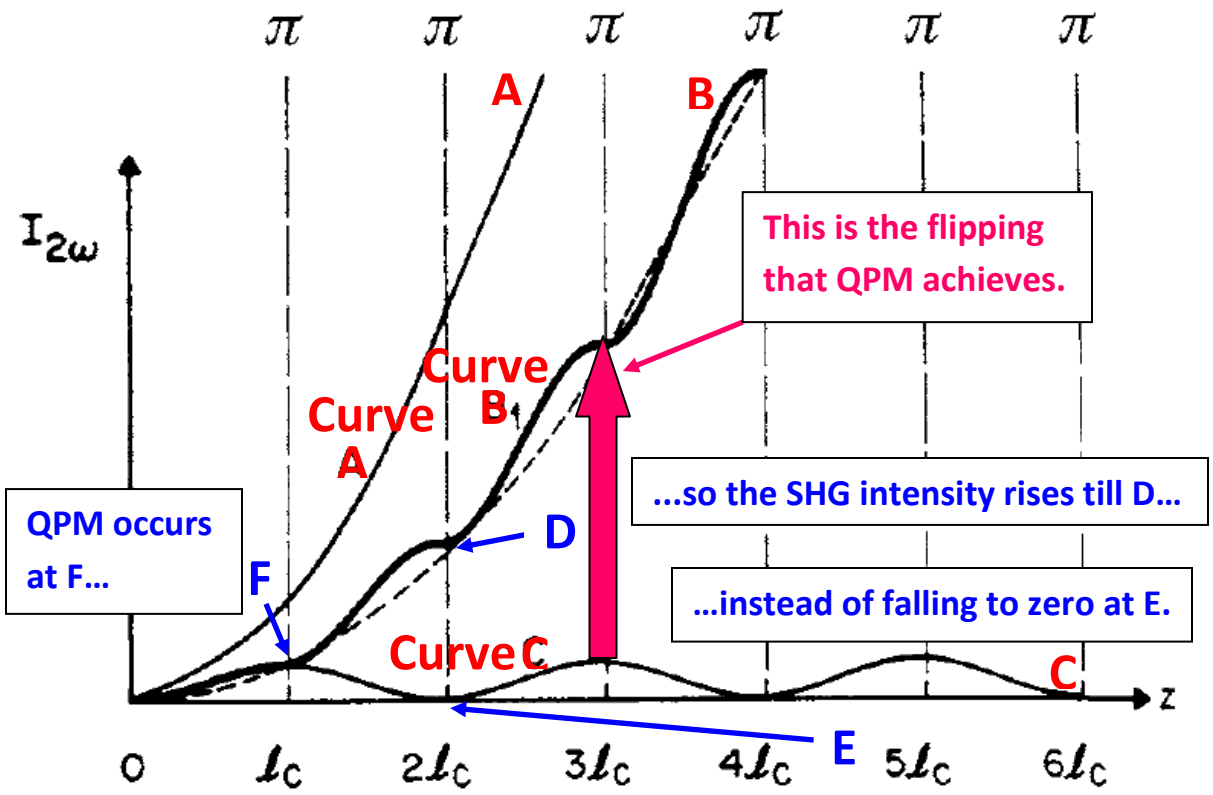

Figure 5: Stepwise build up of second-harmonic power due to QPM. Curve A shows the build up with perfect $\Delta k = 0$ phasematching. Curve B shows the build up achieved with $\Delta k \neq 0$ and QPM, where an additional π phase shift is introduced every unit length l_c by introducing a periodic poling of the nonlinear crystal. Curve C shows the periodic build up and decrease of second-harmonic power with $\Delta k \neq 0$ and no QPM.

The goal of this paper is to generate as much power at the second harmonic as is possible. Hence, we need to scrutinize an equation which yields the second harmonic intensity in terms of various relevant parameters. In other words, we are looking for analytical expressions to quantify the graphs in Figure 5. Risk et al [2] have presented such an expression for SHG intensity as a function of crystal length, amongst others parameters:

$$I(2\omega_1) = \frac{2\pi^2 d_{32}^2}{\lambda_3^2 n_3 n_1^2 \epsilon_0 c_0} * l^2 * I_1^2 * sinc^2\left(\frac{\Delta k l}{2}\right)$$

$$= \alpha * l^2 * I_1^2 * sinc^2\left(\frac{\Delta k l}{2}\right) where\ \alpha = \left(\frac{2\pi^2 d_{32}^2}{\lambda_3^2 n_3 n_1^2 \epsilon_0 c_0}\right) - -(4)$$

where α is a constant incorporating information regarding the crystal and the incident light, l is the crystal length, I_1 is the intensity of the incident light and Δk is as defined in equation (2). Formally, Δk is called the wavevector mismatch. This equation leads to two distinct cases: $\Delta k \neq 0$ (finite wavevector mismatch) and $\Delta k = 0$ (zero wavevector mismatch).

Case 1: $\Delta \boldsymbol{k} = \mathbf{0}$

This occurs in birefringent phasematching; the $sinc^2$ term in equation (4) becomes unity due to its vanishing argument and we have (treating α and I_1 as constants):

$$I(2\omega_1) \propto l^2$$

This is represented in curve A of Figure 5, where the output SHG intensity grows quadratically with crystal length.

Case 2: $\Delta \boldsymbol{k} \neq \mathbf{0}$

For the case of finite wavevector mismatch, we perform some simplification to equation (4):

Treating α and I_1as constants, we get

$$I(2\omega_1) \propto l^2 sinc^2\left(\frac{\Delta k l}{2}\right) = \left(\frac{2}{\Delta k}\right)^2 sin^2\left(\frac{\Delta k l}{2}\right)$$

$$I(2\omega_1) \propto sin^2\left(\frac{\Delta k l}{2}\right) - - - (5)$$

Hence, the second harmonic intensity simply oscillates between zero and a maximum repeatedly, no matter how long the crystal used is. This is represented in curve C of Figure 5.

QPM pertains to case 2 ($\Delta \boldsymbol{k} \neq \mathbf{0}$)**.** However, instead of letting the intensity fall to zero after each unit distance (l_c), we "flip" the curve so that it rises in the opposite. Returning to Figure 5, and comparing curve B with C between l_c and $2l_c$ we see this "flipping" occurring at point F – hence, when z = $2l_c$ the intensity has risen substantially (point D) instead of falling back to zero

(point E). A physical mechanism is needed to accomplish this "flipping," which is the heart of quasi-phase-matching. It is clear that some physical quantity needs to be modulated periodically. What is it, and how often do we flip it (in other words, what is the unit distance l_c mentioned in Figure 5)? These two questions:

What is being periodically modulated?

What is the period of this modulation?

will require a deep dive into QPM theory, which will be discussed next.

The final second harmonic power generated at the output crystal face is a sum of the second harmonic power arising from the infinitesimal waves generated at each point along the crystal. Each point should be seen as a minute antenna. If the waves by each antenna are in phase with each other – in other words, their wavevectors are parallel – the final second harmonic wavevector is the linear sum of all the minute wavevectors generated throughout the crystal, as shown in Figure 6.

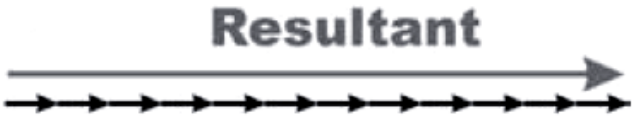

Figure 6: the wavevectors from different points along the crystal are "in phase" (i.e. parallel) with respect to each other, so the final second harmonic wavevector is a direct sum of the individual wavevectors.

Now, we prove the above ideas mathematically. The generated second-harmonic field – in the frequency domain – is given by Risk [2] as:

$$\frac{\partial \tilde{E}_{SHG}(x,\omega)}{\partial x} = \alpha[e^{i(\Delta k)x}\delta(\omega-\omega_3) - e^{-i(\Delta k)x}\delta(\omega+\omega_3)]$$

where α is a constant incorporating parameters associated with the nonlinear crystal and the incident laser beam, ω_3 is the second harmonic frequency and $\Delta\mathrm{k}$ is the wavevector mismatch defined previously. When we integrate over distance i.e. x we obtain a term like $\int e^{i(\Delta k)x}\,dx$ along with its complex conjugate. This term represents the superposition of second-harmonic waves generated at different points in the crystal. The complex number $e^{i(\Delta k)x}$ has magnitude 1

and phase angle $(\Delta k)x$.We can represent this complex number as a phasor of length 1 at an angle $\phi = (\Delta k)x$. For visual clarity, we can approximate the continuous integral $\int_0^l e^{i(\Delta k)x}\, dx$ with a discrete sum:

$$\left(1 + e^{i(\Delta k)\delta x} + e^{i(\Delta k)2\delta x} + e^{i(\Delta k)3\delta x} + \cdots + e^{i(\Delta k)(N-1)\delta x}\right)\delta x = \delta x \sum_{j=1}^{N} e^{i(\Delta k)(j-1)\delta x}$$

where $l = N\delta x$. We can now understand the phasors in Figure 6 better. If $\Delta k = 0$, then $e^{i(\Delta k)\delta x} = 1$ and the integral has its maximum value – that is, that is, all the phasors align in the same direction and add to give the maximum sum, corresponding to perfect constructive interference between second-harmonic contributions from different sections of the crystal. However, if the waves generated at each point are out of phase with each other, there is now an angle between each phasor and its neighbor. In Figure 7(a), there is a slight phase error between the second harmonic contributions from different portions of the crystal, so that perfect constructive interference does not occur and the second harmonic output is reduced.

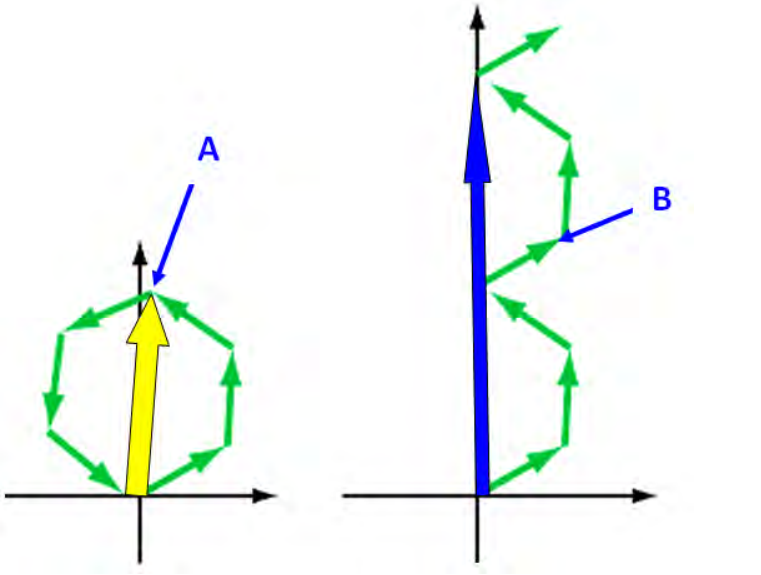

without phase matching **with quasi-phase matching**

Figure 7(a) **Figure 7(b)**

Figure 7: A phasor approach to understanding how QPM helps enhance the second harmonic intensity (see in-text explanation after this for details).

We observe, in Figure 7(a), that it takes six arrows to sum up to nullity. To aid physical intuition, let us attribute each arrow to a molecule; then, for every distance corresponding to six molecules the SHG intensity falls to zero. At three molecules, the wavevector magnitude has just reached a maximum [yellow arrow in Figure 7(a)]. We compare point F in Figure 5 against point A in Figure 7(a) and observe that the they both correspond to maximum intensity. At this point, we would like to flip the arrow at point A by 180^{o} or π radians until it points in the opposite direction as per point B in Figure 7(b); thus, the intensity will continue to rise for the distance equivalent to another three molecules, and the final wavevector after six molecules is represented by the blue arrow in Figure 7(b), instead of zero as in Figure 7(a). This phase shift of π is needed every time a distance of three molecules is traversed by the second harmonic wave, and inducing it is known as quasi-phase matching. The three molecules merely served as an illustrative example; in general, this periodic distance is known as the coherence length. With the insight gained from the preceding phasor analysis, we can recast the two questions previously stated into the following form:

How do we induce a phase shift of π every time a coherence length is traversed?

How long is "one coherence length"?

Starting with the second, the π phase shift needs to be induced whenever the second harmonic intensity is a maximum, such as at point F in Figure 5.

Using the analytical expression for the intensity, equation (5):

$$I(2\omega_1) \propto sin^2\left(\frac{\Delta kL}{2}\right)$$

The intensity of the second harmonic attains its first maxima at

$$\left(\frac{\Delta kL}{2}\right) = \left(\frac{\pi}{2}\right)$$

We define the coherence length $l = l_c$ as the distance traversed by the electromagnetic wave in the crystal medium from entry till the first maxima, whereby:

$$l = l_c = \left(\frac{\pi}{\Delta k}\right).$$

Since the wavevector in the crystal is $k = \left(\frac{2\pi}{\lambda/n}\right)$, where n is the medium refractive index, we have

$$l_c = \left(\frac{\pi}{\Delta k}\right) = \left(\frac{\pi}{2\pi\Delta n/\lambda}\right) = \frac{\lambda}{2\Delta n} = \frac{\lambda}{2|n(2\omega) - n(\omega)|} - - - (6)$$

λ, the pump wavelength (which is twice the desired wavelength) and n, the refractive indices, depend on the material used. Hence, from these two input parameters alone, one can compute the desired coherence length. Equation (6) is identical to that given by Ghatak and Thyagarajan [6] for computing the coherence length in QPM.

In phasor terms, the coherence length l_c just defined corresponds to the distance traversed by the beam in the crystal till the second harmonic intensity reaches point A in Figure 7(a), which is the longest possible net phasor that can exist. Any distance traversed by the beam exceeding l_c implies that the net phasor (yellow arrow in Figure 7(a)) continues rotating anticlockwise past its maximum length, thus declining in length and causing the second harmonic intensity to drop.

How do we induce a phase shift of π every time a coherence length is traversed?

Returning to the first question, we take note that for ferroelectric materials, such as lithium niobate, there exists a threshold temperature (called the Curie temperature) below which a spontaneous electric polarization P_s is present even in the absence of an external electric field. This polarization originates from an internal charge separation due to the atomic arrangement in the crystal. This charge separation defines a direction connecting the negative charge center to the positive one; thus, ferroelectric materials have a “polar axis” that acts as a directional reference by which the crystal can differentiate between an applied electric field that points in the same direction as the spontaneous polarization from one that points in the opposite direction.

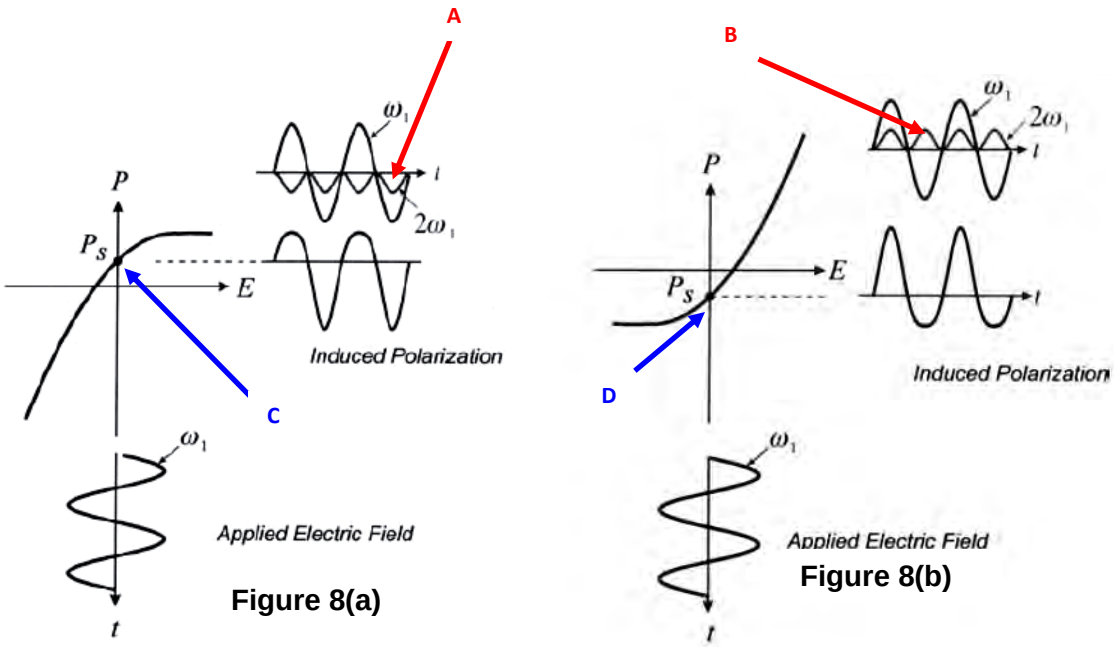

Figure 8(a) **Figure 8(b)**

Figure 8 [2]: A graphical representation of how inverting the spontaneous ferroelectric polarization can induce a phase shift of π radians in the second harmonic wave, which helps enhance SHG efficiency through the QPM mechanism that has been detailed in Figure 5 (graphically) or equivalently in Figure 7 by a phasor plot.

Suppose, at zero applied field, we invert the polarity of the intrinsic polarization from C to D. This induces a π rad phase shift in the second harmonic wave generated, as evidenced by the downward to upward flipping in the $2\omega_1$ wave from A to B.

Figure 8 shows the effect of the spontaneous polarization on SHG. Figure 8(a) is similar to Figure 2, except that in Figure 2, $P = 0$ when $E = 0$, whereas in Figure 8(a), $P = Ps$ when $E = 0$. The applied electric field at fundamental frequency causes a charge separation that adds to and subtracts from the fixed charge separation arising from the spontaneous polarization. In Figure 8, the nonlinear response of the induced polarization has been decomposed into components at the fundamental and second-harmonic frequencies. Figure 8(b) shows the same effect when the direction of the spontaneous polarization is reversed. The second-harmonic components of the two responses are 180◦ out of phase with each other. Hence, if we invert the spontaneous polarization periodically, we have a mechanism for producing the 180◦ phase shift required to implement QPM.

How is a domain-inverted structure with a period as small as tens of micrometers produced in a nonlinear crystal? Currently, the most successful and ubiquitous approach is to deposit a periodic electrode, such as a patterned metal film, on one surface of the crystal (Figure 9(b), blue arrows). A uniform electrode is applied to the opposite surface (Figure 9(b), long red arrow). When a sufficiently large electric field is applied to these electrodes, inverted domains begin nucleating under the regions where the periodic electrode is in contact with the crystal. Under the influence of the applied field, these domains grow until they occupy the area directly under the electrode and extend across the entire crystal thickness. Periodic poling of this nature has been successfully demonstrated in lithium niobate, forming periodically poled lithium niobate (PPLN), which is the crystal to be used for this current project.

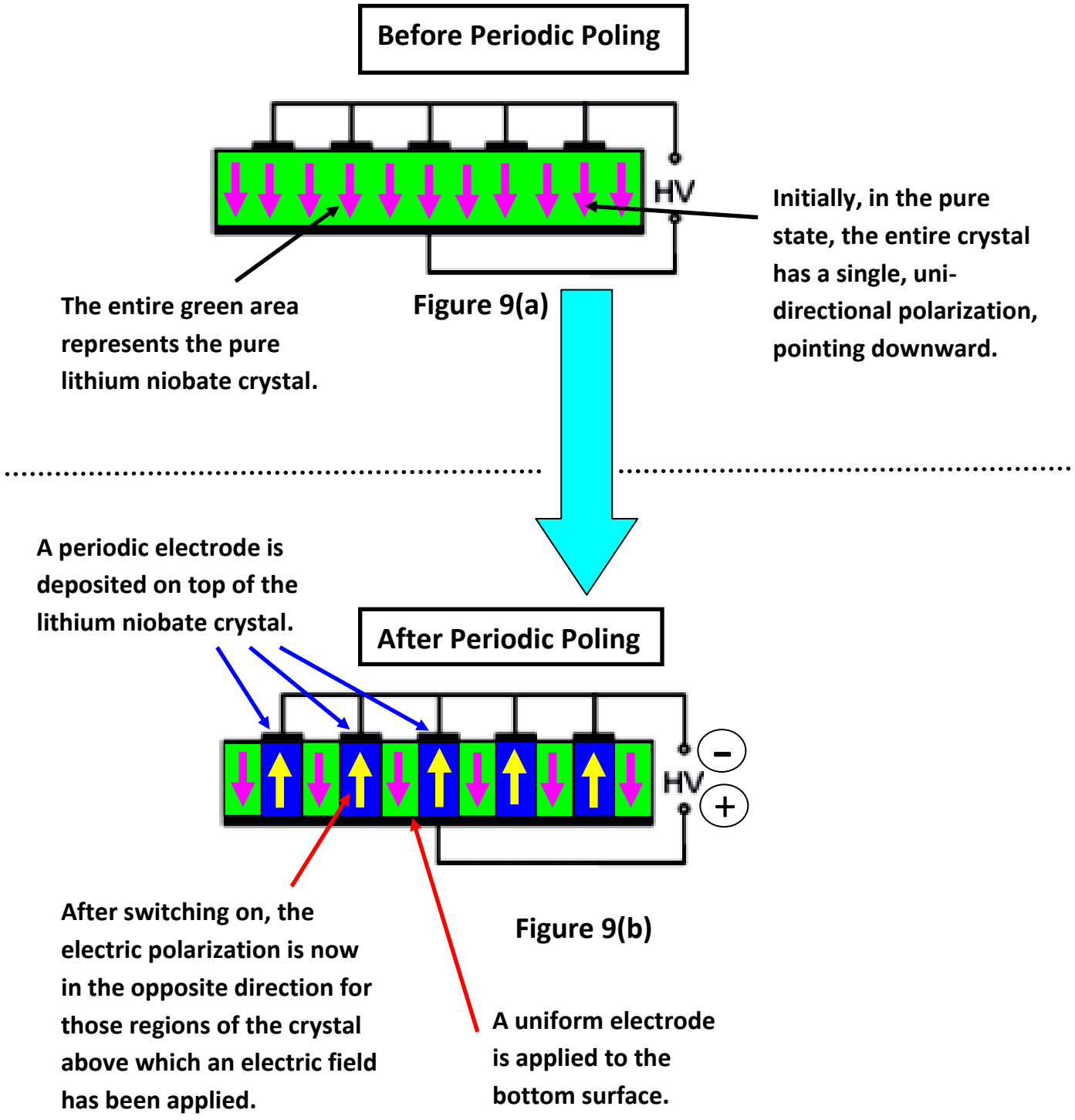

Figure 9: An overview of the electric field poling process to produce periodically-poled crystals.

4. Factors affecting efficiency of Second Harmonic Generation

Previously, we have looked at the basic principles of QPM. We now focus on one aspect which is the goal of this project: to convert as much of the incident power at the fundamental frequency into its second harmonic. Hence, the conversion efficiency, as defined by $Power_{\boldsymbol{out}}(2\omega)/\ Power_{\boldsymbol{in}}(\omega)$ is an appropriate benchmark by which our performance can be gauged. To achieve the aforementioned target, a theoretical analysis will be performed to identify, comprehend and implement factors (listed immediately below) which would maximize the conversion efficiency.

4.1 Temperature and poling period
4.2 Boyd-Kleinman focusing factor
4.3 Input power
4.4 Polarization
4.5 Photorefractive effects
4.6 Number of longitudinal modes
4.7 Location of beam focus

4.1 Temperature and poling period

We start off with the first factor. For QPM, a unique poling period is needed for every wavelength. Deviation from this poling period would not maximize the conversion efficiency [5]. However, our periodically-poled crystals came with fixed periods of 19.20µm, 19.50µm, 19.80µm, 20.10µm and 20.40µm, none of which corresponded to our target wavelength (of 1560 nm). Hence, temperature tuning is performed whereby thermal expansion of the crystal lengthens its poling period slightly, thereby allowing a broader range of wavelengths to be converted efficiently. The temperature-length relationship is governed by the linear thermal expansion coefficient of lithium niobate [7]:

$$\frac{\Delta l}{l} = (1.59 * 10^{-5})(\Delta T) + (4.9 * 10^{-9})(\Delta T)^2$$

$$where\ \Delta T = T - 25^{o}C\ and\ l\ is\ the\ unexpanded\ length\ of\ a\ single\ poling\ period$$

$$\therefore \Delta l = l[(1.59 * 10^{-5})(\Delta T) + (4.9 * 10^{-9})(\Delta T)^2]$$

$$length\ of\ a\ poling\ period\ after\ thermal\ expansion \equiv\ \mathcal{L}(T) = l + \Delta l$$

$$= l[1 + (1.59 * 10^{-5})(\Delta T) + (4.9 * 10^{-9})(\Delta T)^2] - - - (7)$$

Returning to equation (6),

$$\frac{\lambda}{2|n(2\omega) - n(\omega)|} = l_c - - - (6)$$

we define the poling period $\mathcal{L}(T)$ as twice the coherence length l_c (Figure 10):

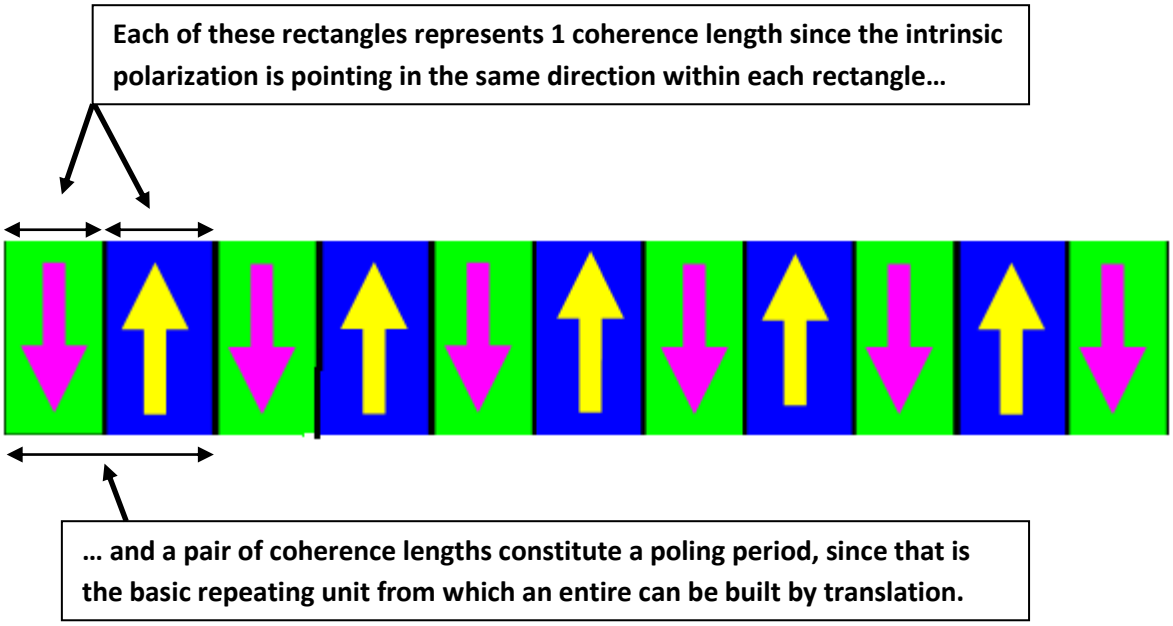

Figure 10: An illustration of why the poling period is twice the coherence length.

and thus rewrite equation (6) as follows:

$$\frac{\lambda}{|n(2\omega) - n(\omega)|} = \mathcal{L}(T) - - - (8)$$

Now, we make explicit what was being suppressed earlier, which is the temperature-dependence of the refractive index (compare the arguments of equations 8 and 9):

$$\frac{\lambda}{|n(2\omega, \boldsymbol{T}) - n(\omega, \boldsymbol{T})|} = \mathcal{L}(T) - - - (9)$$

In truth, the temperature of a medium also affects its refractive index – indirectly – by altering its density. A higher temperature causes the density of the medium to fall and become less viscous, allowing light to travel faster in it which yields a smaller refractive index. The converse happens as temperature falls.

By varying the temperature, both the left-hand side (LHS) and the right-hand sides (RHS) of equation (9) are changing. For the LHS, the refractive indices are functions of temperature and wavelength through the Sellmeier equations, whereas the poling period increases monotonically with temperature on the RHS. The temperature at which the above relation attains equality is the phasematching temperature. To solve the equation, and thereby derive the phasematching temperature, we bring forth the Sellmeier equation, which relates the wavelength λ and temperature to the refractive index n as follows [8]:

$$n = \sqrt{a_1 + b_1 * f + \frac{a_2 + b_2 * f}{\lambda^2 - (a_3 + b_3 * f)^2} + \frac{a_4 + b_4 * f}{\lambda^2 - (a_5)^2} - a_6} - - - (10)$$
$$where\ f = (T - 24.5^O C)(T + 570.82)$$

The values of the Sellmeier coefficients (a_1 to b_4) are tabulated in Appendix 1.

We now substitute equations 7 and 10 into 9:

$$\left| \sqrt{a_1 + b_1 * f + \frac{a_2 + b_2 * f}{{\lambda_1}^2 - (a_3 + b_3 * f)^2} + \frac{a_4 + b_4 * f}{{\lambda_1}^2 - (a_5)^2} - a_6} - \sqrt{a_1 + b_1 * f + \frac{a_2 + b_2 * f}{{\lambda_2}^2 - (a_3 + b_3 * f)^2} + \frac{a_4 + b_4 * f}{{\lambda_2}^2 - (a_5)^2} - a_6} \right|$$
$$= \frac{\lambda}{l[1 + (1.59 * 10^{-5})(\Delta T) + (4.9 * 10^{-9})(\Delta T)^2]} - - - (11)$$

Theoretically, this equation can be solved since only the temperature is unknown, but being a transcendental function forbids analytical solutions. It is apt to exploit a numerical method, such as the Newton-Raphson's iterative procedure, to solve for the root of the equation, which would give the phasematching temperature for a particular wavelength. This procedure should then be repeated for a list of wavelength values, whilst holding the poling period ι (in the denominator of the RHS) constant. This would give a list of values describing how the phasematching temperature varies with the wavelength for a single unexpanded poling period (consider any one column in Figure 11, from 19.2 μm

to 20.4 μm). The entire process can then be repeated for another value of the unexpanded poling period, which would give another list. In Figure 11, we offer a sample of values representing numerical solutions for equation (11); as expected, there are five lists, each representing a different poling period.

1	Numerical solutions to the phasematching equation (11) for tempertature						
2							
3		Temperature	19.20μm	19.50μm	19.80μm	20.10μm	20.40μm
4		30	1543.692	1554.785	1565.701	1576.313	1587.199
5		36.12	1544.689	1555.4	1566.315	1577.166	1588.099
6		40.2	1545.234	1555.995	1566.8	1577.614	1588.539
7		47	1545.827	1556.874	1567.598	1578.333	1589.382
8		50.4	1546.417	1557.308	1568.087	1578.896	1589.745
9		53.8	1546.817	1557.695	1568.621	1579.387	1590.362
10		57.2	1547.229	1558.237	1569.04	1579.954	1590.958
11		60.6	1547.627	1558.593	1569.792	1580.194	1591.269
12		64	1547.98	1559.103	1569.949	1581.002	1591.739

Figure 11: Sample values showing numerical solutions to equation (11).

Since this table is critical to the entire QPM business, it is worth interpreting in detail. Consider the box shaded in red, which is read as follows: to maximize the conversion efficiency of a 1555.4 nm incident beam, the crystal is translated laterally until the beam is striking the 19.5 μm channel, but this latter period is still insufficient; hence, the temperature is raised to 36.12 °C whereby the poling period expands slightly until it attains the ideal phasematching value such that equation (11) is satisfied. Under such conditions, the incident light will be converted with maximum efficiency into its frequency-doubled harmonic.

For this paper, we should be looking at values near the 1560 nm spectral range. Using equation (11) again, we obtained the following approximate temperatures:

Temperature/°C	**Unexpanded Poling Period/μm**
143.29	19.2
72.36	19.5

Table 2: Relevant combinations of temperature and unexpanded poling periods for efficient conversion of 1560 nm pump wavelength

Hence, if the initial unexpanded poling period of 19.20 µm (or 19.50µm) is used, the optimal temperature for quasi-phase-matching is expected to be approximately 143^{o}C (or 72 ^{o}C); these values are based on equation (11). However, some deviation between these numerically-computed values and the empirically-derived ones is expected, since it would not be possible to practically reproduce those perfect conditions as were assumed in the calculations. For instance, the incident beam needs to strike the crystal head-on, at normal incidence (see Figure 22); however, this may not be fulfilled practically due to the difficulties associated with aligning the beam on such a microscopic crystal. In addition, the calculations assume a perfect crystal of alternating upward- and downward-pointing domains of equal length (Figure 10), but due to imperfections in the periodic poling process, certain domains may not be poled correctly leading to irregular structures like:

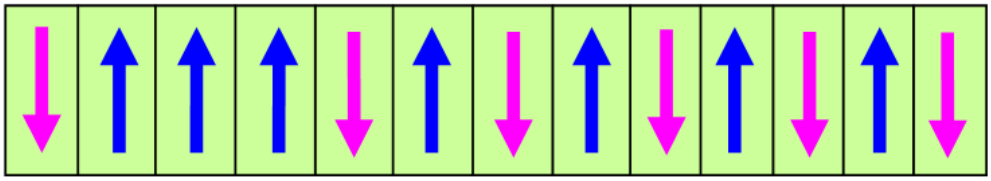

Figure 12: An imperfect PPLN crystal where the third domain failed to invert downward.

Such defects can occur in the poling process because the electrodes to be deposited on the crystal are only tens of micrometers long, and a number of errors can arise in the lithographic printing process dealing with such microscopic resolution. For instance, if the temperature of the deposition chamber is not set correctly – either due to equipment or human error – the electrodes may fail to deposit at a certain location where they were supposed to; consequently there will be no inversion of polarization at that location leading to an incorrectly-poled structure.

Defects such as that in Figure 12 lead to a change in the effective poling period encountered by the incident beam, such that the new (i.e. effective) poling period does not correspond to the old phasematching temperature for a given input wavelength. This explains why differences may arise between the computed and empirical phasematching temperature, due to a variety of experimental (alignment issues) and engineering (such as crystal defects) reasons.

It is the goal of this paper to empirically establish the optimum temperature for the relevant poling period. Nonetheless, the equations (and their numerical solutions) are a potent tool to illuminating the

underlying mechanism; in addition, by foretelling the expected optimal temperatures, they shorten the discovery time by allowing the researcher to home in on the correct temperature more swiftly.

4.2 Input power

Secondly, the conversion efficiency is increased by raising the pump power (at fundamental frequency). As the latter increases, the second harmonic power exhibits a quadratic increase. Boyd and Kleinman [9] have derived the relationship between the input (fundamental frequency) power and second harmonic power under optimum focusing conditions (these focusing conditions will be discussed in the next section):

$$P_{out} = 1.068 \frac{16\pi^2 d_{eff}^2}{\epsilon_0 c \lambda_1^3 n_1 n_3} P_{in}^2 l \quad ---(11A)$$

$$\therefore P_{out} \propto P_{in}^2$$

We return to equation (1):

$$\boldsymbol{P_{nonlinear}(t) = \epsilon_0 \left[\chi^{(1)} E(t) + \chi^{(2)} E(t)^2 + \chi^{(3)} E(t)^3 + \cdots \right]} \quad ---(\mathbf{1})$$

and consider only the second-order nonlinear polarization, $\boldsymbol{P_{nonlinear}^{(2)}(t)}$, which causes SHG:

$$\boldsymbol{P_{nonlinear}^{(2)}(t) = \epsilon_0 \left[\chi^{(2)} E(t)^2 \right]} \quad ---(\mathbf{12})$$

We now offer a simple argument to explain why the output power is quadratically – and not linearly – proportional to the input power. We know that the input intensity is proportional to the amplitude of the input electric field squared ($\boldsymbol{E(t)^2}$), which is in turn proportional to the second-order nonlinear polarization $\left(\boldsymbol{P_{nonlinear}^{(2)}}\right)$ from equation 12. Hence, by doubling the input power, we double the intensity as well since area is assumed constant throughout. Therefore, $\boldsymbol{P_{nonlinear}^{(2)}(t)}$, as well as the amplitude of the second harmonic electric field, doubles; the latter quantity causes the output SHG intensity to increase fourfold. Hence, an increase of input power results in a quadratic increase in the SHG power generated.

4.3 Boyd-Kleinman focusing factor

Thirdly, we explore the best way to focus the beam into the crystal in order to maximize SHG power. Boyd and Kleinman (1968) [9] have explained how this is done.

In the ideal case, if laser beams did not diverge at all, one simply has to focus the beam as tightly as possible to obtain the smallest spot size. In this case, the average intensity across the entire crystal length is maximized and thus the SHG output is also maximized (it has been demonstrated qualitatively in the preceding section that the SHG power increases quadratically with the input power).

In practice, we use Gaussian beams that diffract in the plane transverse to the propagation direction. The more tightly the beam is confined, the more rapidly it will diffract. Hence, the high-intensity region is confined to a small area near the beam waist, and it will not be possible to maintain that confinement over a very long length. Equation (4) shows that the interaction length directly determines the conversion efficiency; thus, we are forced to accept a trade-off between tight confinement and long interaction length. Hence, for a crystal of a fixed length, there is an optimum focusing condition that represents a compromise between tight confinement and long interaction length. It is this condition that is known as the Boyd-Kleinman focusing condition (see equation (13)).

To aid intuition, imagine that if the spot size is too small, the beam has been focused very tightly and thus it will diffract faster spatially in the plane transverse to the propagation direction.. Hence, whilst the intensity at the minimum beam waist is high, the intensity at the other points in the crystal will be much lower and consequently the average intensity integrated over the entire crystal will also be low leading to a low conversion efficiency. On the other hand, if the spot size is too large, the beam diffracts less but the average intensity of the incident beam along the entire crystal will again be low, since it was low at every point along the crystal to begin with. Somewhere in between, a compromise is struck where the spot size is neither excessively large nor too small, at which the intensity attains a maximum.

However, Boyd and Kleinman (1968) [9] did not specify optimized values for spot size; rather, they analysed the issue from the complementary viewpoint, which is the degree of divergence, as quantified by the confocal parameter (confocal parameter = 2 x Rayleigh length). The link between the spot size and the confocal parameter is as follows: the smaller the spot size, the faster the beam will diffract spatially and the shorter the confocal parameter.

Their analysis culminated in the following relation, the Boyd-Kleinman focusing condition:

$$L/b = 2.84 - - - (13)$$

where L is the crystal length and b is the confocal parameter. For this paper,

$$b = \frac{L}{2.84} = \frac{40.0}{2.84} = 14.08mm$$

$$Rayleigh\ length\ = \frac{14.08}{2} = 7.04\ mm$$

From laser focusing theory, if a collimated Gaussian beam with beam radius w_0 hits a focusing lens with focal length f, the beam radius at the beam waist w_f (minimum spot size) is given by:

$$w_f = \frac{\lambda f}{\pi w_0}$$

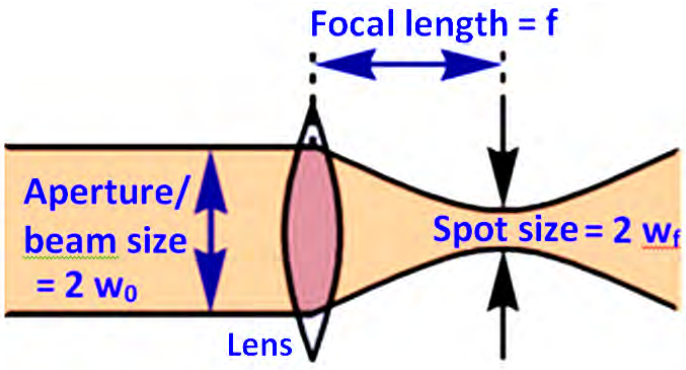

Figure 13: An illustration of the various parameters involved in laser focusing: the minimum spot size w_f achievable is determined by the incident beam size $2w_0$, the wavelength λ and the focal length f.

The Rayleigh range is:

$$z_R = \frac{\pi w_f^2}{\lambda} = \frac{\pi}{\lambda}\left(\frac{\lambda f}{\pi w_0}\right)^2 = \frac{\lambda}{\pi}\left(\frac{f}{w_0}\right)^2$$

$$f = \sqrt{\frac{\pi\, z_R w_0^2}{\lambda}} = \sqrt{\frac{\pi * 7.04 * 10^{-3} * (0.55 * 10^{-3})^2}{\lambda}} = 65.5\ mm$$

Hence, a converging lens of focal length 65.5 mm is appropriate for our set-up, which corresponds to a beam waist of 29.6 mm. We used the closest available lens (50 mm), which represents a beam waist of 22.6 mm.

4.4 Polarization

The polarization state of the input beam directly affects the SHG efficiency. When the incident electromagnetic wave propagates through the crystal, its electric field component induces rapid oscillations in the lithium niobate dipoles provided there is effective coupling between the two. Hence, there is maximum energy transfer from the incident field to the oscillating dipoles, which consequently begins radiating at the second harmonic with maximum efficiency. The incident electromagnetic wave must drive the nonlinear polarization $P^{(2)}$. Therefore only the electric field component in this direction is contributing. Mathematically, $P^{(2)} \propto cos^2\theta$, where is the relative angle between the plane containing the lithium niobate dipole and the electric field. The maximum value is obtained by letting $\theta = 0^o$, which makes the two preceding planes parallel. Hence, maximum SHG power occurs by aligning the polarization plane of the incident beam parallel to the dipole moment vector of the crystal.

4.5 Photorefractive effects

Table 2 reveals that one can use two temperatures for a 1560 nm pump wavelength, provided the poling period is changed accordingly. This generates an extra degree of freedom in optimizing the input parameters. Photorefractive effects degrade SHG efficiency more strongly at low than at high temperatures. Hence, exploiting this new degree of freedom implies choosing that poling period at which the higher crystal temperature is involved. For our case, this implies using the 19.5 μm poling period at 142°C.

The mechanism of photorefractive degradation is as follows: at low crystal temperatures, intensity-dependent refractive index effects deteriorate the spatial beam quality since the beam intensity distribution follows a Gaussian profile. Hence, different points – in the pane transverse to beam propagation – in the crystal experience different laser intensities, and consequently different refractive indices, via two distinct mechanisms: thermal effects and photorefractive effects.

Firstly, thermal effects occur as the intensity distribution (and heating rate) within the crystal varies spatially, so the beam encounters slightly different refractive indices at different points (the Sellmeier equations (10) relate the temperature dependence of refractive indices); hence, the spatial quality of the beam degrades, leading to lower average beam intensity throughout the crystal. Since the second harmonic power generated is dependent on the average squared intensity integrated across the crystal, the former decreases at low temperatures.

Secondly, photorefractive effects achieve a similar spatially-dependent refractive index. The spatially-dependent beam intensity alters the local space-charge distribution by a spatially-dependent electron photo-excitation rate. This results in charge migration from locations of high to low electron density, which generates a position-dependent electric field and refractive index (via the electro-optic effect) [10].

The net effect of the two processes is that the beam encounters a spatially-dependent refractive index. This degrades its spatial quality since the beam refracts unpredictably, leading to an overall decrease in average beam intensity throughout the crystal and the consequent decrease in second harmonic power generated.

Recent theoretical computations by Guohui et al [11] have suggested that the second factor dominates the first, though Jedrzejczyk et al [12] and Louchev et al [13] offer a contrasting viewpoint. We have been unable to verify either claim due to an inability to measure the temperature or refractive index distribution within the small crystal. However, the real cause is not important since the ultimate observable effect on the beam is exactly the same – spatial profile degradation.

On the other hand, if the temperature is high, the uniform thermal heating from the oven largely overwhelms any minute spatial differences in heating rates caused by the non-uniform intensity profile of the Gaussian beam. The entire crystal is at a uniform temperature, and photorefractive effects do not adversely affect the maximum intensity attainable. The preceding ideas are well-evidenced by the scatter plot obtained by Peil et al [1]:

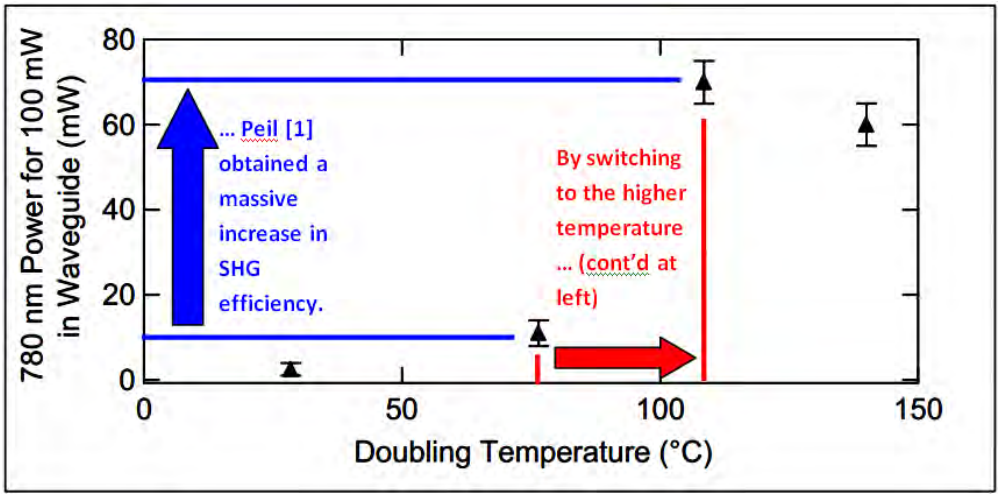

Figure 14: Experimental results from Peil et. al. [1] showing the adverse effects (in the form of much lower efficiency) of performing SHG at low temperatures (compare the first two and last two points) owing to photorefractive effects. By using the channel with a higher (i.e. >100°C) phasematching temperature (see red arrow), the SHG efficiency rose from approximately 10% to 70% (see blue arrow).

Hence, maximum SHG conversion efficiency is attained by minimizing photorefractive effects

5 Experimental set-up of SHG apparatus

We now look at the various components of the SHG set-up we constructed.

The DFB semiconductor seed laser generates a weak (2-4 mW) 1560 nm narrow linewidth beam that is fed into the erbium-doped fiber amplifier for power enhancement up to 20W. A visible laser is injected and combined with the invisible infrared beam using a polarizing beam splitter so that the latter becomes visible and easy to manipulate spatially. A half-wave plate is inserted next to control the polarization of the beam entering the crystal. After that, the PPLN crystal is placed in an oven for temperature tuning; the oven is sandwiched by two converging lenses – the first one for focusing the beam into the crystal such that the minimum beam waist coincides with the crystal's geometrical center, and the second one for collimating the beam leaving the crystal to ensure that it possesses a good (Gaussian) spatial quality. Next, the beam Is filtered – by a dichroic mirror – into the (desired) second harmonic (780 nm) component and the residual, unconverted pump beam (1560 nm). The former is injected into a Rubidium cell for frequency stabilization and locking, before being coupled to a long-range fiber optical cable for transmission to the experiments.

A schematic outline of our set-up is presented in Figure 15.

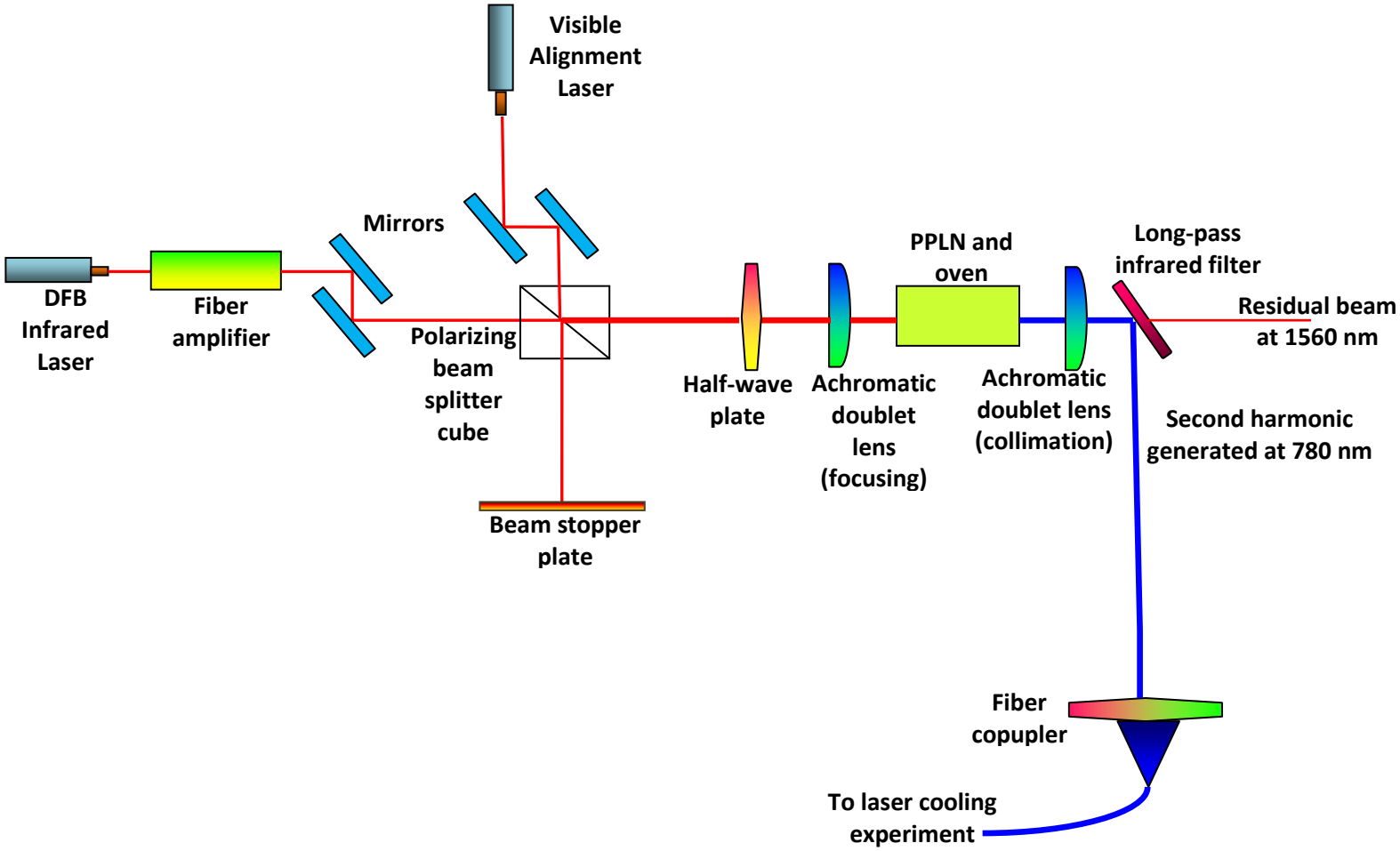

Figure 15: A schematic outline of the various components that constitute our SHG set-up.

6 In-depth analysis of each component

In this section we look at each component in detail to study the role it plays in generating SHG output. This would also signal areas for improvement and offer clues as to which of the factors are most critical in achieving our target i.e. high SHG efficiency.

6.1 Seed laser

A distributed feedback (DFB) laser is used as the source laser for subsequent amplification and frequency doubling. The key advantage of the DFB laser used is the narrow linewidth of 100 kHz. To perform spectroscopy on the atoms, the laser frequency must match the rubidium transition frequency as closely as possible, which can be practically achieved by using a laser with a narrow linewidth.

Besides a narrow linewdith, it is critical to ensure that the laser frequency and the rubidium frequency are centered at the same value. It is pointless to speak of a narrow linewidth if the laser is lasing at, say, 1561 nm and the atomic transition line is centered at 1556 nm, for instance. In this case, there will be little coupling between the laser photons and the atoms. For the rubidium cooling, the D2 transition line at 780.24 nm will be utilized. Hence, the DFB laser must also be engineered to lase at this value. The laser can then be temperature-tuned over a spectral width of approximately 1-2 nm to home in on the precise frequency of 780.24 nm. We opted to center our DFB laser at 1560 nm, giving us a range of operation of roughly 1559-1561 nm; this spectral range contains double of the desired rubidium D2 transition line (780.24 nm).

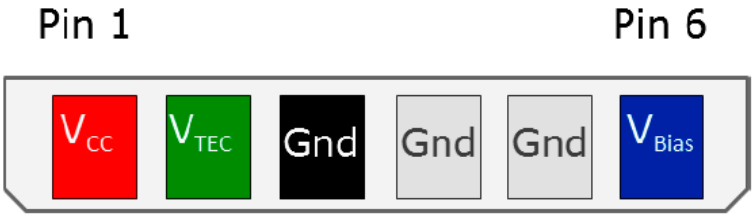

Figure 16: A screenshot from the manufacturer's datasheet showing the various wire colorings and their respective uses.

The DFB laser arrived as a standalone module without any power supply unit. Simply put, there were six bare wires (Figure 16) dangling from the laser module so a circuit board was designed to supply the laser with a reliable and safe source of electricity.

Each of the six wires serves a purpose:

Pin 1: Supplies the baseline voltage of +5V to the laser

Pin 2: Variable voltage (0.1 – 3V) to control the temperature of the laser, which allows a slow tuning in the interval 1559 – 1561 nm

Pin 3-5: Grounded

Pin 6: Variable voltage (0 – 2.5V) to control the bias current through the laser, which controls the laser power and allows fast frequency tuning.

The circuit components in Figure 17 were soldered onto a circuit board to supply the laser with its electrical power requirements.

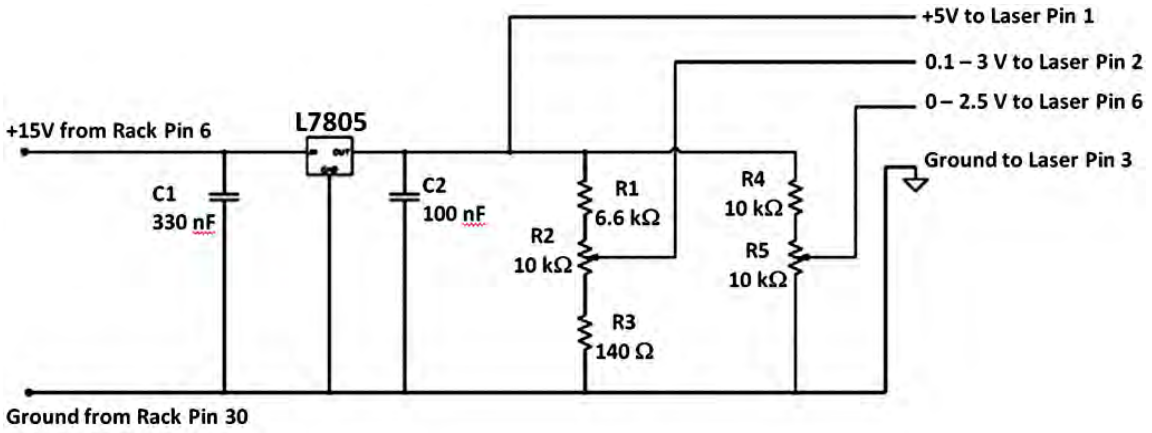

Figure 17: An electric circuit diagram representing the power supply unit for the DFB laser

Prior to wiring and firing up the laser, it is essential to test it using a multimeter to ensure that all output voltage values fall within the range specified by the manufacturer. It would be disastrous if the voltages are in large excess of the recommended values, which may trigger a current surge that might incapacitate the delicate components inside the laser. However, a voltage value slightly lower than specified is not a material issue as it simply means that the laser may not be operating at full power.

Circuit board performance

Laser Pin	Ideal Voltage (V)	Measured Voltage (V)	Result
1	5.00	5.02	Pass
2(min)	0.100	0.043	Pass
2(max)	3.000	2.982	Pass
6(min)	0.000	0.000	Pass
6(max)	2.500	2.412	Pass

Table 3: A report of how our circuit board fared in comparison to the values specified by the laser manufacturer.

All the measured values are generally close to what has been specified by the manufacturer, except for a few minor deviations. The only significant discrepancy lies in the minimum value of pin 2, whose minimum value fell to 0.043 V, significantly lower than the 0.100 V specified. This occurred as a 140 Ω

resistor could not be found, so a 150 Ω resistor was used instead; consequently, the voltage sharing ratios were adversely affected, which manifested in the aforesaid anomaly. However, since the discrepancy is negative, the risk of current surges leading to fried laser components is negligible. The core of the circuit is the L7805 voltage regulator, which provides an extremely stable output voltage of +5 V. In addition, to minimize the likelihood of overheating and a potential meltdown, the laser module was attached to a multi-fin heat sink, as per Figure 18, and the entire combination was screwed onto an empty circuit board, before being slotted into an electrical rack.

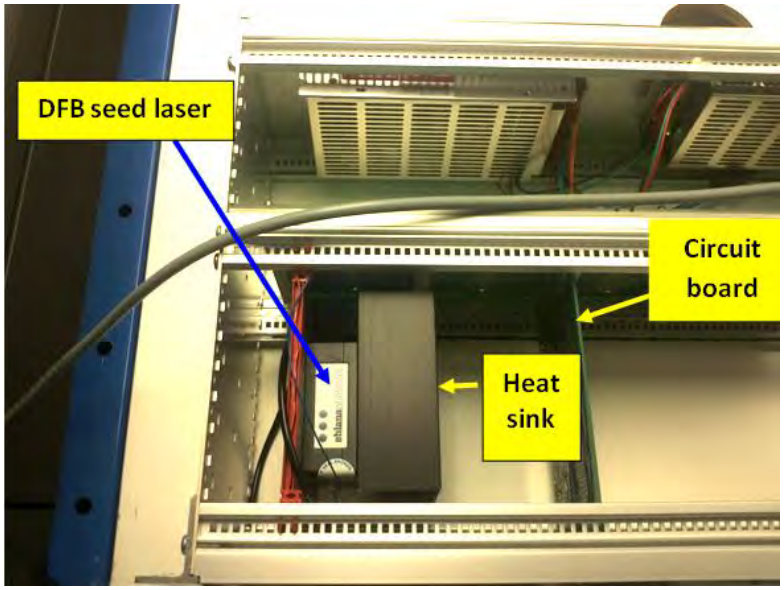

Figure 18: The laser module and heat sink are shown here and the entire package was placed in a rack for stability.

6.2 Fiber Amplifier

A typical setup of a simple erbium-doped fiber amplifier (EDFA) is shown in Figure 19. The core of the amplifier is the erbium-doped single-mode optical fiber, which is pumped with light from two laser diodes (bidirectional pumping).

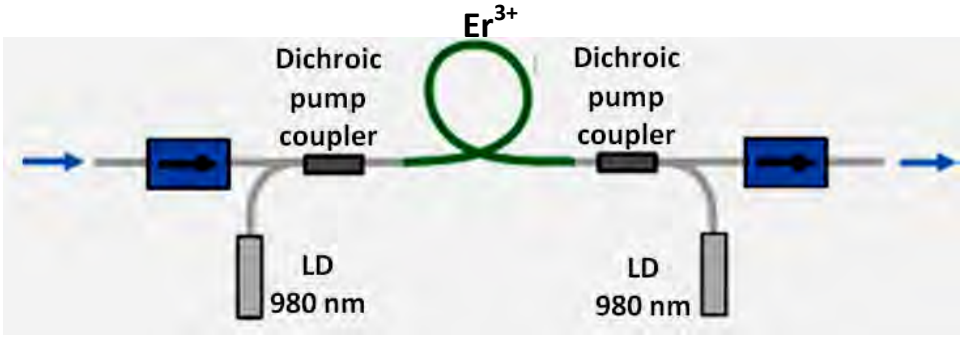

Figure 19: A schematic outline of the essential components of an erbium-doped fiber amplifier is shown, including the two pumping laser diodes (LD 980 nm) and the active gain medium which is a single-mode erbium-doped (Er^{3+}) fiber.

The relevant energy levels of erbium are shown in Figure 20. The amplifier pump laser operates at 980 nm, which causes excitation of the erbium atoms from the $4I_{15/2}$ to the $4I_{11/2}$ state [Figure 20, step 1], followed by a fast phononic decay to the $4I_{13/2}$ state [Figure 20, step 2] – which has a relatively long mean lifetime, as occurs in meta-stable states – which can subsequently amplify light in the 1.5-µm wavelength region via stimulated emission back to the ground-state manifold $4I_{15/2}$ [Figure 20, step 3].

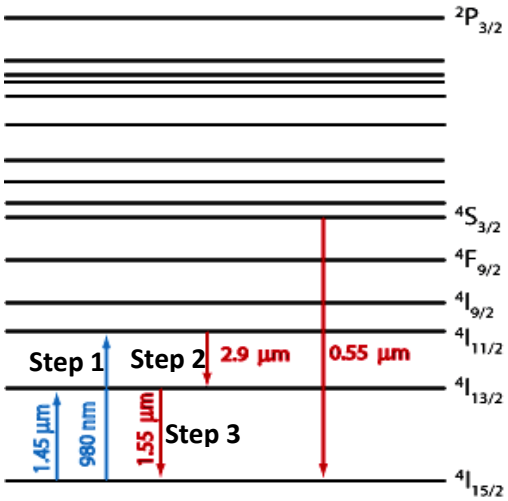

Figure 20: An energy-level diagram of the various electronic states of erbium.

An interesting observation we made regarding the fiber amplifier is its nonlinearity of output with respect to input. The front-panel screen on the amplifier allows power tuning from 1% to 100%, which theoretically corresponds to powers of 0.2W to 20W (maximum possible output). Contrary to expectations, the amplifier began lasing at 0.63W even at 1%. This is a safety hazard as an unsuspecting user may insert optical components that are designed for, suppose, powers below 500 mW, in which

case the components may sustain irreversible damage. The most likely explanation for this anomalous behavior is the existence of a threshold power below which lasing cannot occur. Besides the abovementioned issue, the fiber amplifier is relatively hassle-free to operate.

The singular concern which expended the greatest amount of time is the risk of back-reflections obliterating the amplifier. Generally, the issue revolves around inadvertently placing reflective components like mirrors in front of the amplifier, which may cause the high-powered beam emerging from the amplifier to flood back into it, and thus the circulating power within the amplifier may exceed its damage threshold. Two solutions were studied for this purpose: (a) a faraday isolator and (b) a quarter-wave plate (QWP) in series with a polarizing beamsplitter (PBS) (see Figure 21). For solution (b), any back-reflected beam (point A) is constrained to execute a double pass through the QWP, leading to a $\lambda/2$ – phase shift by the time it returns to the PBS (point B), thus forcing it to reflect harmlessly away (path C) from the optical path returning directly to the fiber amplifier (path D).

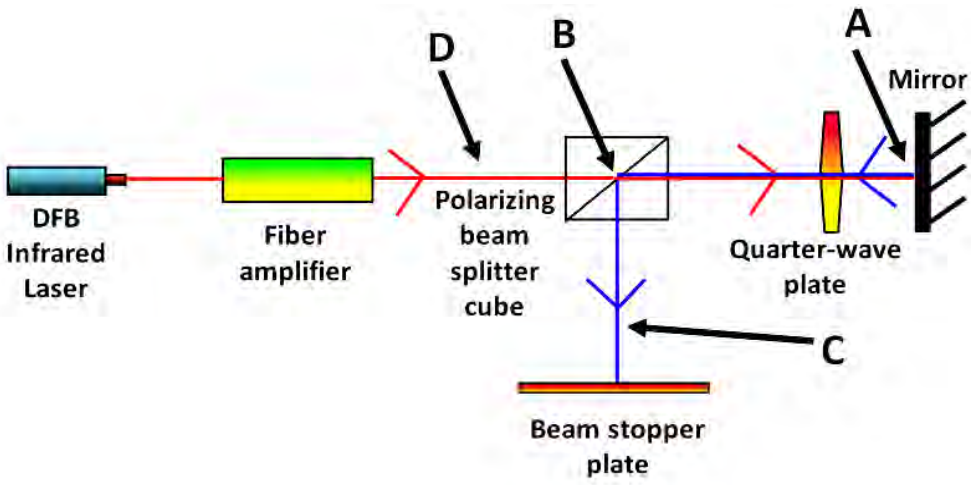

Figure 21: An illustration of how a QWP in series with a PBS can channel back-reflected light (blue lines) away from the optical path heading directly back to the amplifier, in case reflective components like mirrors are inadvertently placed in front of the beam.

Unfortunately, both solutions were ultimately rendered unsuitable and we proceeded without either. A suitable faraday isolator could not be found that could withstand power levels of 20W, whilst a quarter-wave plate generates circularly-polarized light that is grossly inappropriate for frequency doubling. The latter demands light that is polarized linearly along the dipole moment plane (see Section 6(d)), and circularly-polarized light has a negligible component along the aforesaid plane. Before switching on the

amplifier, we proceeded with a fundamental analysis of the entire set-up to identify potential sources of back-reflections. All transitive optics used (Figure 15) were anti-reflection coated whose coating's maximum transmittance lies in the 1050 – 1620 nm spectral region. Such anti-reflection coating is classified as C-class coating by Thorlabs. At 1560 nm, the reflectance for C-class coated dichroic mirrors is approximately 0.03%, so the maximum possible back-reflection is below 6 mW. The amplifier itself is equipped with a built-in isolator that offers protection against back-reflections up to -30 dB, which should generally be able to handle the aforesaid 6 mW of back-reflections without causing any optical damage to the amplifier. The most critical elements are the lenses that focus and re-collimate the beam, which have the greatest amount of anti-reflection coating compared to smaller optics. Using optics with the wrong coatings can be disastrous as it can have a relatively high reflectance at the incident wavelength, thus causing the beam to be back-reflected. This is why we chose such anti-reflection coating whose spectral range includes our operating wavelength of 1560 nm.

6.3 Frequency doubling apparatus – oven and PPLN crystal

The temperature tuning for the PPLN crystal is to be performed using an internally-designed oven. The oven is the housing for the PPLN crystal. Besides adjusting the crystal temperature, it offers physical protection for the crystal (see Figure 23), which is essential considering the cost of the crystal. Undoubtedly, the key performance indicator for the oven is its long-term temperature stability, which is elaborated fully in Section 7. Here we look at another issue related to the oven. The critical part of the project is ensuring that the incident beam from the amplifier actually passes through the correct channel within the crystal out of 5 available channels, since only one is usable for a particular temperature. The entry face of each channel has an area of approximately (1 x 1) mm^2 and the beam's diameter is about 0.8 mm upon entering a channel. There is a very narrow tolerance range for positioning the beam, which means that a slight deviation from the ideal position would result in a decline in second harmonic output. Hence, the beam must be normally incident at the correct channel (second channel from top of Figure 22(a)), so that it passes through that channel for the entire crystal length. Also, the beam should not straddle several channels diagonally (Figure 22(c)), as then the frequency doubling process would not be occurring along the entire crystal length and the second harmonic output is sub-optimal. Neither should the beam be incident at the intervening space between

two channels, for then little SHG is expected since the effective interaction length during which the beam traversed the correct channel is almost negligible (Figure 22(b)).

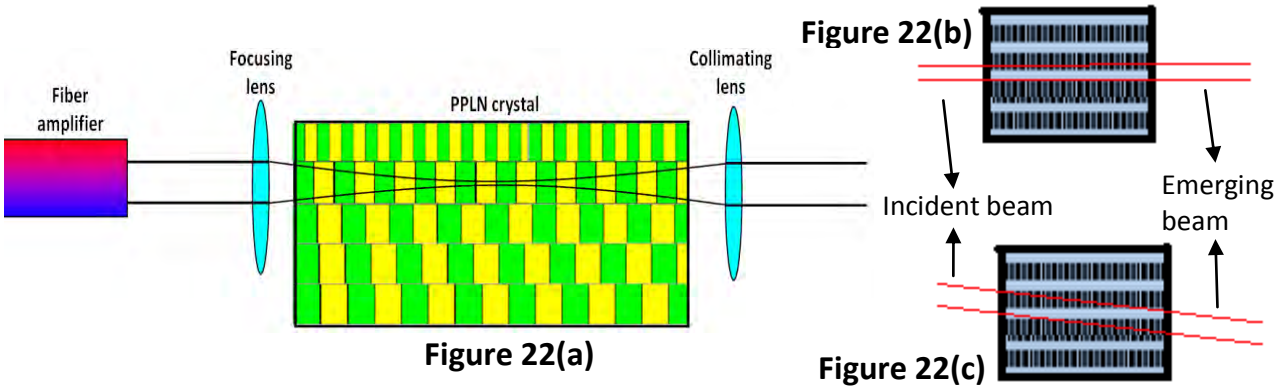

Figure 22: (a) The primary challenge is in ensuring that the incident beam passes through the correct channel (second channel from top) for the entire length of the crystal. (b) If the beam is not incident at the channel's center, it may intrude onto the next channel since the channels are closely spaced and (c) if the angle of incidence is non-normal, the beam would travel diagonally across multiple channels even if it entered the correct channel.

The guiding principle latent within the aforementioned discourse is that the second harmonic intensity is proportional to the effective interaction length (equation (4)), which is the spatial extent for which the beam is traversing through the correct channel. This demands very precise control of the position of the oven, for which we have employed a positioning stage upon which the oven is mounted (Figure 23).

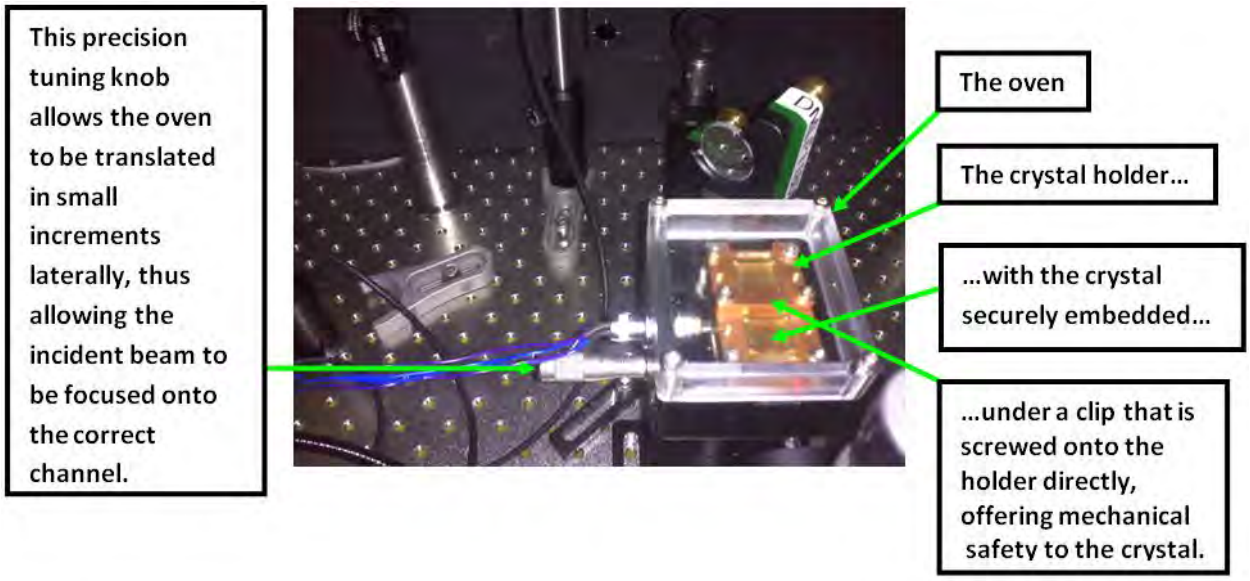

Figure 23: The oven is mounted onto a positioning stage, whose knob allows fine lateral translations, which is crucial to align the beam onto the correct channel as illustrated in Figure 22(a).

6.4 Alignment laser

The incident infrared laser (λ =1560 nm) is invisible to the naked eye. Therefore, before aligning the infrared beam to the crystal (as discussed immediately above), it is necessary to mark its position, for which a few options were considered.

Firstly, an infrared-viewing telescope set was used in an attempt to observe the beam. Whilst this is an innovative approach, it must be used with some caution. Alignment work in optics is usually done at low power levels (in our case, perhaps 1% of full amplifier power, approximately 650 mW). However, at such low levels, the beam has a low scattering – and visibility – within the crystal. The beam traversing the crystal becomes visible in the IR viewer when the amplifier power exceeded 20% ($\tilde{}$5 W), and it is slightly hazardous to perform optics alignment work with such high powers. Secondly, when placing an infrared detector card near the crystal to detect the position of the beam. This caused minute sparks to be produced, and this practice was deemed grossly unsuitable due to the risk of contaminating the crystals with residues from the detector card. The focused laser beam was so intense that it caused some

combustion of the chemicals within the card. Hence, the detector card technique could not be used as a long-term, reliable way of marking the invisible beam. The safest and least costly technique was to inject an overlapping visible laser beam into the optical path of the invisible beam. As long as both beams overlap perfectly, the visible beam can be used as a marker to align the invisible beam onto the right crystal channel. The trickiest part is ensuring that the two beams actually overlap, which was accomplished with the aid of two irises (Figure 24). After that the alignment beam is used to position the optics.

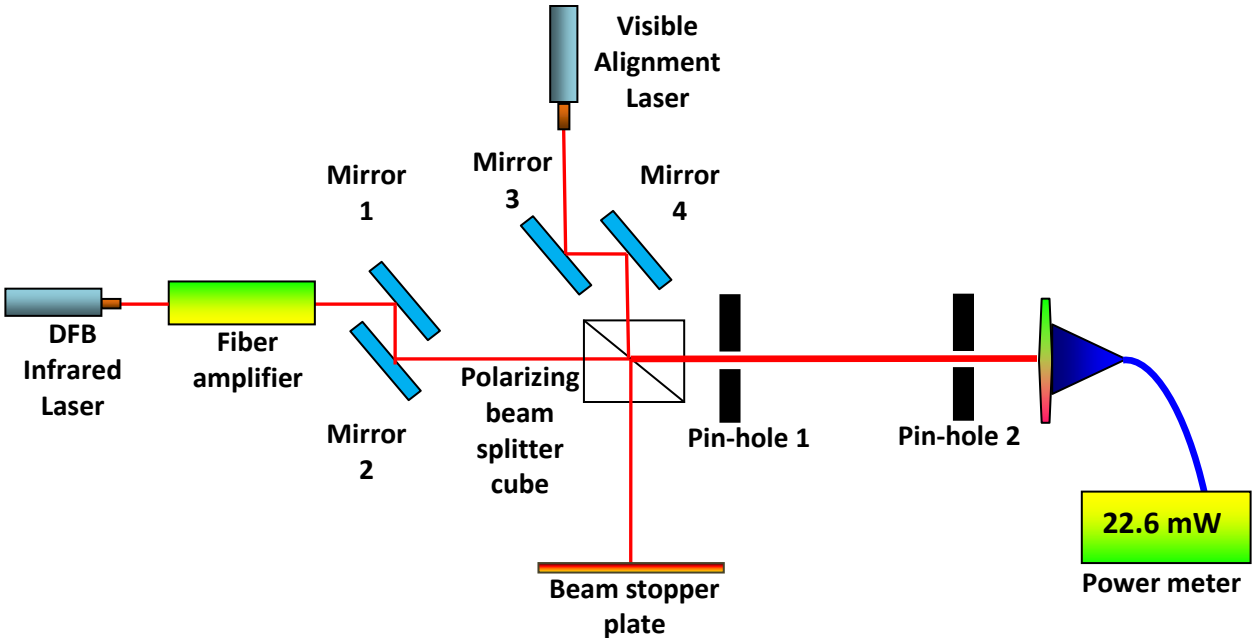

Figure 24: The two irises are used to align the visible and invisible beam with each other, after which the invisible beam can be positioned using the visible one as a marker.

Hence, the crystal can now be positioned using the visible beam alone, as shown in Figure 25.

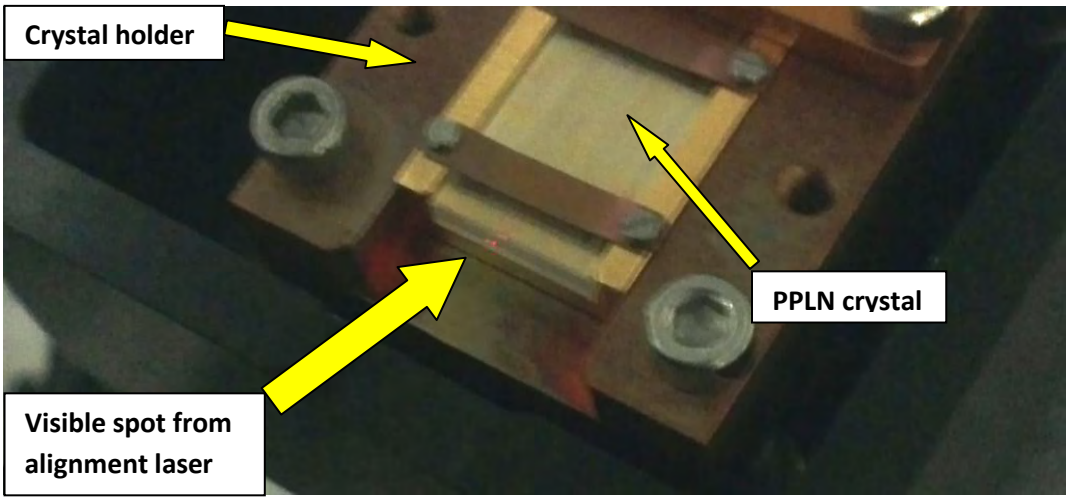

Figure 25: The crystal with a red spot from the visible alignment laser beam. The spot can be seen because the anti-reflection coating on the entry face of the crystal is optimized for spectral values in the vicinity of 780 nm and 1560 nm, and reflects/scatters 650 nm rather well, allowing it to be detected by the human eye.

7 Experimental results

In this chapter, I will describe the experimental results that I obtained during the course of this project.

7.1 Temperature Bandwidth

Firstly, we look at the temperature acceptance bandwidth curves for our crystal. The temperature acceptance bandwidth is calculated from the full-width at half maximum (FWHM) of the SHG intensity-temperature plot. In other words, we are trying to calculate the amount by which the temperature must deviate from the optimum value before the SHG power falls to half its maximum value. We denote twice this value as the temperature bandwidth $\equiv \Delta T_{HWFM}$. This is a crucial quantity as it would offer an estimate of how tightly the crystal temperature must be controlled to ensure no significant power degradation at the second harmonic.

The temperature tunes the phasematching condition though thermal expansion. As the temperature rises, the crystal expands and the poled periods' length increase slightly. The new period no longer corresponds to the optimum value for the pump wavelength (of 1560 nm); rather the new period corresponds to some new value for the wavelength. However, since the incident light is monochromatic, the net result is that the conversion efficiency at the original pump wavelength decreases. This is why the ΔT_{HWFM} is a crucial quantity for benchmarking the performance of any SHG set-up.

We have obtained the following graphs for the temperature acceptance bandwidth near 80°C, using a poling period of 19.5μm and near 150°C, using a poling period of 19.2μm:

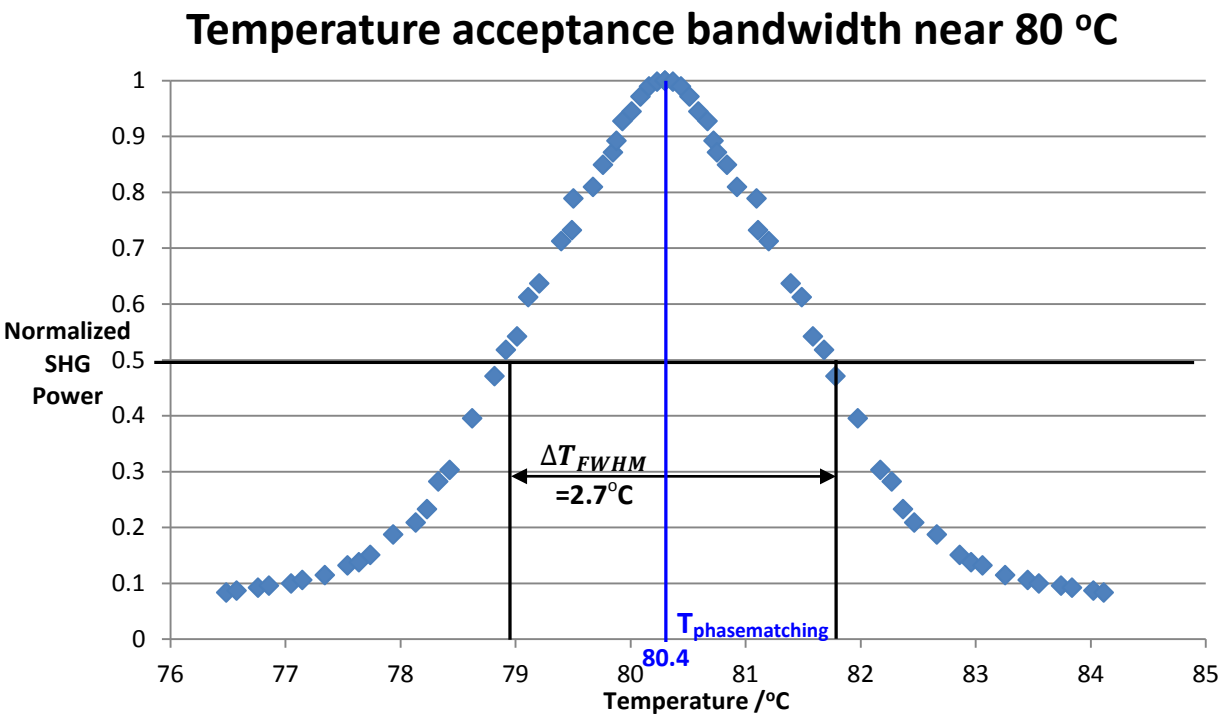

Figure 26: The SHG Power v Temperature plot we obtained near 80°C using a period of 19.5 μm.

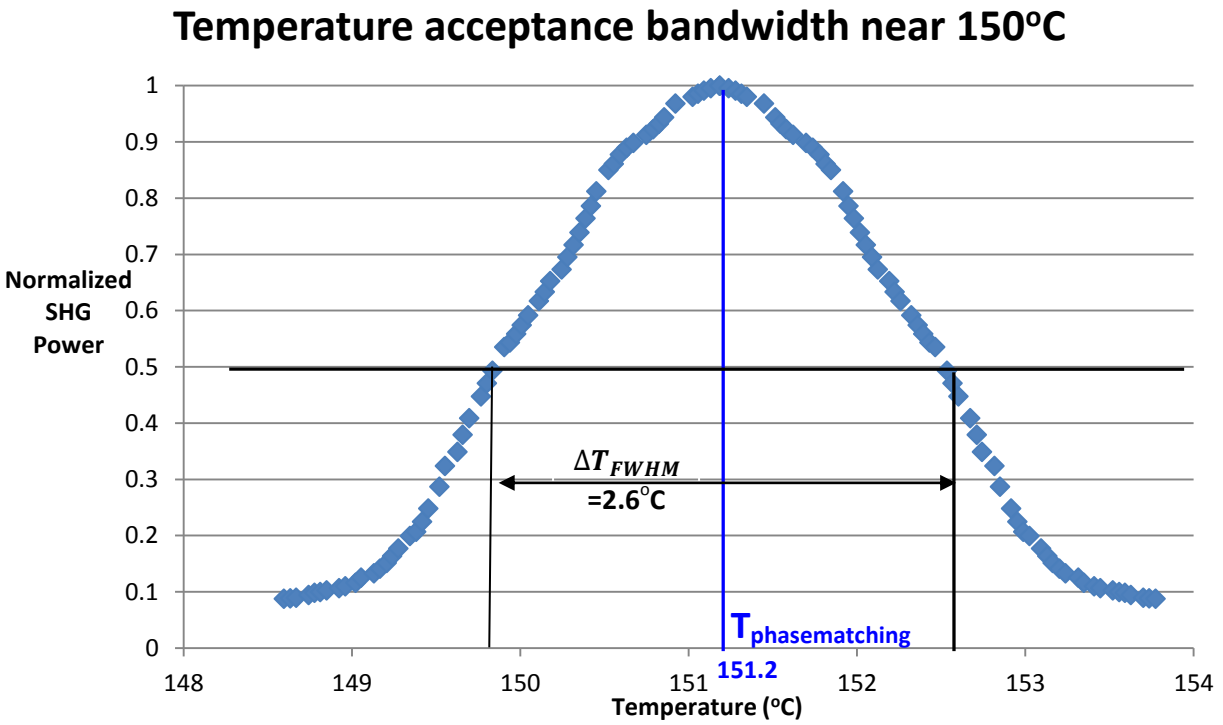

Figure 27: The SHG Power v Temperature plot we obtained near 150°C using a period of 19.2 μm.

We now derive a theoretical value for the FWHM temperature bandwidth near 80°C based on a formula given by Risk et. al. [5]: (this formula has been derived in detail by Fejer et. al. [4])

$$\Delta T_{FWHM} = \left| \frac{1.39\lambda_{pm}}{\pi l \left[\left(\frac{\partial n_3}{\partial T} - \frac{\partial n_1}{\partial T} \right)_{T=T_{pm}} - \alpha(n_3 - n_1) \right]} \right|$$

The values of the refractive indices are obtained from the Sellmeier equations given by Gayer et. al. [8]

$$n^2 = a_1 + b_1 * f + \frac{a_2 + b_2 * f}{\lambda^2 - (a_3 + b_3 * f)^2} + \frac{a_4 + b_4 * f}{\lambda^2 - (a_5)^2} - a_6$$

$where\ f = (T - 24.5^O C)(T + 570.82)$ and coefficients a_1 - b_4 are given in Appendix 1.

$$for\ T_{pm} = 80.4^o C,\ f = (80 + 570.82)(80 - 24.5^O C) = 36120.5$$

$$n_1 = 2.144\ (for\ \lambda = 1560\ nm)$$

$$n_3 = 2.185\ (for\ \lambda = 780\ nm)$$

Before we obtain the ΔT_{FWHM}, we need to derive an expression for $\frac{dn}{dT}$, starting from

$$n^2 = a_1 + b_1 * f + \frac{a_2 + b_2 * f}{\lambda^2 - (a_3 + b_3 * f)^2} + \frac{a_4 + b_4 * f}{\lambda^2 - (a_5)^2} - a_6$$

$$2n\frac{dn}{dT} = b_1 * \frac{df}{dT} + \frac{d}{dT}\left[\frac{a_2 + b_2 * f}{\lambda^2 - (a_3 + b_3 * f)^2}\right] + \frac{b_4}{\lambda^2 - (a_5)^2}\frac{df}{dT}$$

$$\frac{dn}{dT} = \frac{1}{2n}\left[b_1 * \frac{df}{dT} + \frac{d}{dT}\left[\frac{a_2 + b_2 * f}{\lambda^2 - (a_3 + b_3 * f)^2}\right] + \frac{b_4}{\lambda^2 - (a_5)^2}\frac{df}{dT}\right]$$

It now remains to find an expression for $\frac{df}{dT}$:

$$\frac{df}{dT} = \frac{d}{dT}[(T - 24.5^O C)(T + 570.82)] = 2T + 546.32$$

Hence,

$$\frac{dn}{dT} = \frac{1}{2n}\left[b_1 * (2T + 546.32) + \frac{d}{dT}\left[\frac{a_2 + b_2 * (f)}{\lambda^2 - (a_3 + b_3 * f)^2}\right] + \frac{b_4}{\lambda^2 - (a_5)^2}(2T + 546.32)\right]$$

Now, we evaluate the middle term in the preceding equation:

$$\frac{d}{dT}\left[\frac{a_2 + b_2 * (f)}{\lambda^2 - (a_3 + b_3 * f)^2}\right] = \frac{d}{df}\left[\frac{a_2 + b_2 * (f)}{\lambda^2 - (a_3 + b_3 * f)^2}\right]\frac{df}{dT}$$

$$= \frac{df}{dT}\left[\frac{b_2 * (\lambda^2 - (a_3 + b_3 * f)^2) - \big(a_2 + b_2 * (f)\big)(-2)(a_3 + b_3 * f) * b_3}{(\lambda^2 - (a_3 + b_3 * f)^2)^2}\right]$$

$$= (2T + 546.32)\left[\frac{b_2 * (\lambda^2 - (a_3 + b_3 * f)^2) - \big(a_2 + b_2 * (f)\big)(-2)(a_3 + b_3 * f) * b_3}{(\lambda^2 - (a_3 + b_3 * f)^2)^2}\right]$$

Hence,

$$\frac{dn}{dT} = \frac{2T + 546.32}{2n}\left[b_1 + \left[\frac{b_2 * (\lambda^2 - (a_3 + b_3 * f)^2) - \big(a_2 + b_2 * (f)\big)(-2)(a_3 + b_3 * f) * b_3}{(\lambda^2 - (a_3 + b_3 * f)^2)^2}\right] + \frac{b_4}{\lambda^2 - (a_5)^2}\right]$$

By substituting in the values for the coefficients a_1 to b_4, and f = 36120.5, λ = 1560 x 10^{-9} m and T = 80.4°C, we obtain:

$$\frac{dn_1}{dT} = 1.04853 * 10^{-5}$$

$$\frac{dn_3}{dT} = 3.11285 * 10^{-4}$$

α is the linear thermal expansion coefficient as given by Kim and Smith (1969) [7]:

$$\alpha = (1.59 * 10^{-5})\Delta T + (4.9 * 10^{-5})(\Delta T)^2 \; where \; \Delta T = T - 25^o C$$

$$\therefore \alpha = (1.59 * 10^{-5})(55) + (4.9 * 10^{-5})(55)^2 = 8.89 * 10^{-4}$$

Hence, $\Delta T_{FWHM} = \left| \frac{1.39\lambda_{pm}}{\pi l\left[\left(\frac{\partial n_3}{\partial T} - \frac{\partial n_1}{\partial T}\right)_{T=T_{pm}} - \alpha(n_3 - n_1)\right]} \right| = \left| \frac{1.39\lambda_{pm}}{\pi * 40\left[\left(\frac{\partial n_3}{\partial T} - \frac{\partial n_1}{\partial T}\right)_{T=T_{pm}} - \alpha(n_3 - n_1)\right]} \right| = 1.8^o C$

Our empirically-obtained temperature bandwidth at FWHM is 2.7°C, moderately close to the 1.8°C obtained from theoretical considerations. The deviation in the bandwidth can be explained by the same reasons that the empirical phasematching temperature differs from theoretical computations (see Section 4.1). Primarily, the issue revolves around misaligning the beam onto the crystal at non-normal incidence which causes the beam to encounter an effective poling period that is slightly different from the actual value used in computations. Just as this affects the phasematching temperature, so will it affect the temperature bandwidth. This is because even slight misalignment will cause the beam to encounter an incorrect poling period – and consequently a sub-optimal SHG power – at each temperature value. Hence, the bandwidth, which is simply the width of the SHG power v temperature curve, is also inaccurately determined.

7.2 Polarization

Next, we look at the role of varying the input polarization on the conversion efficiency.

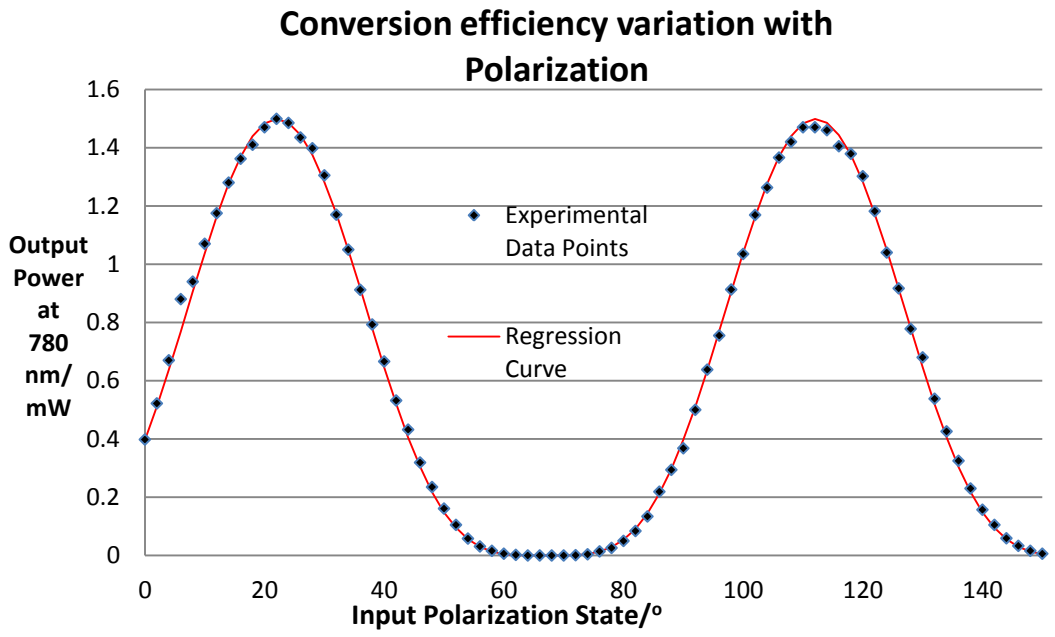

Figure 28: The SHG Power v Polarization plot we obtained near 80°C using a period of 19.5 μm

A highly periodic function is clearly visible, with the conversion efficiency peaking every time the half-wave plate is rotated by about 90°. For our data, the first (and second) peak occur at 22.0° (and 111.0°) respectively, giving a period of approximately 89°. At these orientations of the half-wave plate, the polarization axis of the half-wave plate coincides exactly with the dipole moment of the nonlinear polarization generated within the nonlinear crystal (see Section 4.4).

The peaks are expected to repeat every 90° because a half-wave plate uses birefringent materials as $\lambda/2$ - phase retarders. Hence, every rotation of the HWP by 90° from an intensity maxima rotates the polarization state of the output beam by 180°, which causes maximum coupling between the incident light and PPLN crystal since they are aligned in a vectorially parallel fashion. This generates the largest nonlinear polarization within the PPLN crystal which produces the strongest second harmonic field. The intensity minima occur when the HWP is rotated by 45° from an intensity maximum, so the output beam is rotated by 90°; hence, the output beam polarization is perpendicular to the crystal dipoles and no coupling occurs since a horizontal field cannot exert a vertical force.

The trigonometric least-squares regression curve for our data points is:

$$\boldsymbol{P(\theta) = 1.499 sin^{4.00}(2.00\theta + 0.8)}$$

We would like to analyse this regression function, to predict how the output SHG power depends on the input pump power (the experimental data for this is given in the following section).

We make the assumption that, for the beam, its $power \propto intensity$, since the area of the incident beam is fixed. Malus' law states:

$$I = I_0 cos^2(\alpha) \therefore P = P_0 cos^2(\alpha)$$

based on the aforementioned assumption. Now, theoretical considerations dictate that $P_{out} \propto P_{in}^2$, but we would like to verify this fact experimentally, so we let:

$$2 \longrightarrow \beta$$

$$\therefore P_{out} \propto P_{in}^{\beta} \propto (P_0 cos^2(\alpha))^{\beta} \propto cos^{2\beta}(\alpha)$$

The first proportionality relates the power exiting the crystal to the power entering it and based on the above substitution, the latter's exponent changes from 2 to β. The second proportionality is simply Malus' law, except that the analyser (HWP) precedes the polarizer (PPLN) as per Figure 29. By P_{in},

reference is not being made to the magnitude of the power along path A (Figure 29). Even if the HWP is rotated, the power along A is constant, and only its polarization is changing. Rather, by P_{in} we are referring to the amount of power along path A that effectively couples to the PPLN crystal. This coupling is dependent on the relative directions of the PPLN dipoles and the polarization state of the beam at A. It is this coupling that invokes Malus' law, explaining the second inequality. These powers – P_o, P_{in} and P_{out} – are portrayed in Figure 29.

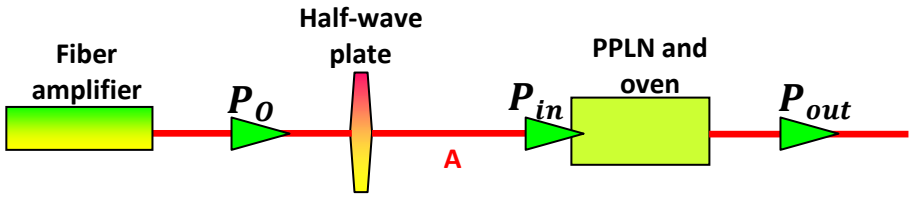

Figure 29: A schematic outline of the various powers mentioned in the preceding paragraph.

Hence,

$$P_{out} \propto cos^{2\beta}(\alpha) = sin^{2\beta}(\alpha + \gamma)$$

where γ is a phase factor that translates the sine curve into its corresponding cosine. Comparing $sin^{2\beta}(\alpha + \gamma)$ with the regression equation, we deduce $\beta = \frac{4.00}{2} = 2.00$. Hence our experimental data proves the theoretical relationship $P_{out} \propto P_{in}^2$ very well. In the following section, we look at the explicit data relating the input and output power.

7.3 Input Power

Now, we present the explicit data relating the power generated at the second harmonic (780 nm) as a function of the input (fundamental frequency at 1560 nm) power. This was measured at 80.4 °C using a poling period of 19.5 μm.

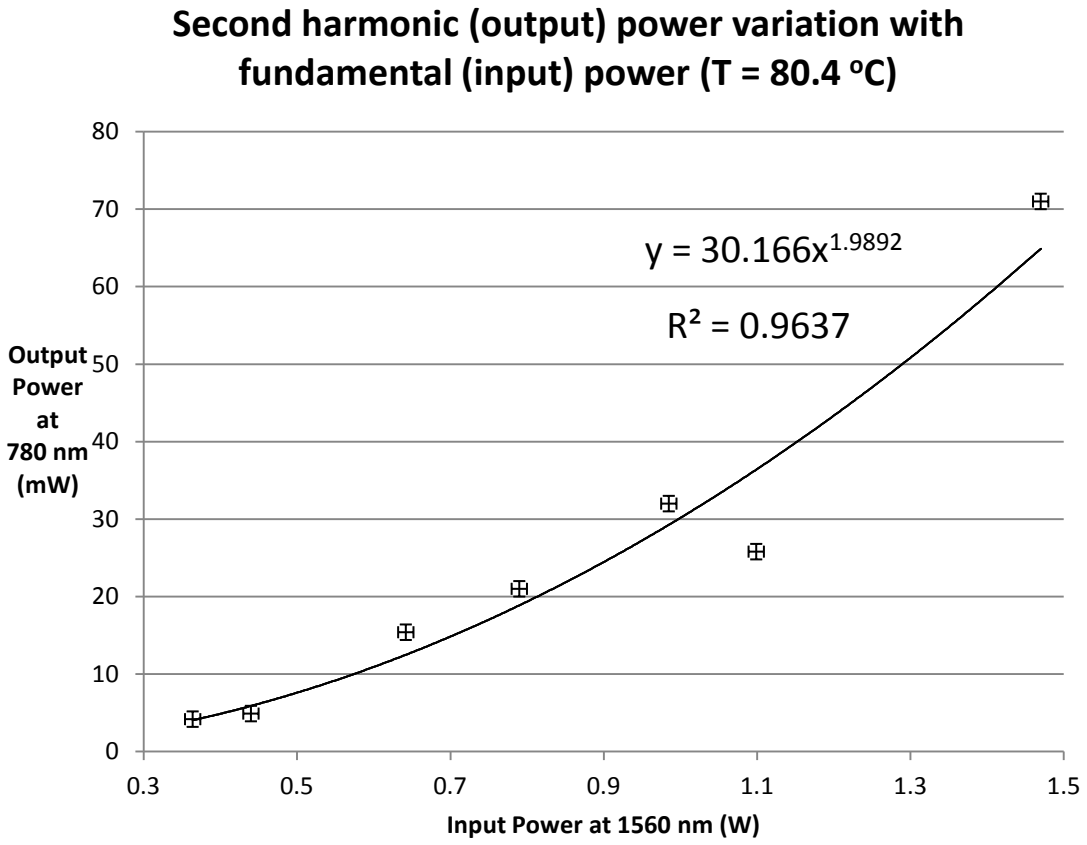

Figure 30: The SHG Power v Input Power plot we obtained near 80°C using a period of 19.5 μm

As the pump power (at fundamental frequency) increases, the second harmonic power exhibits a quadratic increase, as evidenced by a strong positive correlation coefficient when regression analysis was used to fit the experimental data to a power-law curve. The quadratic regression curve is visually a good fit for a majority of the data points, which is based on well-grounded theoretical computations. Recall equation 11A:

$$P_{out} = 1.068\frac{16\pi^2 d_{eff}^2}{\epsilon_0 c\lambda_1^3 n_1 n_3} P_{in}^2 l \propto P_{in}^2 \quad ---(11A)$$

$$\therefore P_{out} \propto P_{in}^2$$

which yields the theoretical relationship between the input (fundamental frequency) and the second harmonic power under optimum focusing conditions. This quadratic relationship is reproduced to a reasonable degree by the data we obtained above, and is in agreement with that discovered by Sane et al [15].

Here we can conclude that our set-up should produce an SHG output of:

$$P_{SHG}(in\ mW) = 30 * P_{in}^{1.9892}\ (in\ W)$$

We have obtained a value of 1.9892 for the exponent, in comparison to the theoretical value of 2. Now, let us estimate the uncertainty associated with 1.9892 using equation 11A.

$$P_{out} = 1.068\frac{16\pi^2 d_{eff}^2}{\epsilon_0 c\lambda_1^3 n_1 n_3}P_{in}^2 l - - - (11A)$$

Firstly, we lump all the constants into α. By constant, we do not mean that the quantity is always invariant (such as crystal length, which is patently not upon heating), but we assume that sufficient relaxation time has been given to allow the system to equilibriate. Hence:

$$P_{out} = \alpha\frac{P_{in}^2}{\lambda_1^3}$$

We now change the exponent of P_{in} to an arbitrary parameter β in order to estimate the uncertainty associated with it:

$$P_{out} = \alpha\frac{P_{in}^{\beta}}{\lambda_1^3} \qquad \therefore \frac{P_{out}\lambda_1^3}{\alpha} = P_{in}^{\beta}$$

Taking base-10 logarithm on both sides and making β the subject, we get:

$$\log P_{in}^{\beta} = \log\left(\frac{P_{out}\lambda_1^3}{\alpha}\right) \therefore \beta\log P_{in} = \log\left(\frac{P_{out}\lambda_1^3}{\alpha}\right) \& \boldsymbol{\beta} = \log\left(\frac{P_{out}\lambda_1^3}{\alpha}\right) / \log P_{in}$$

Define $\log(P_{out}\lambda_1^3/\alpha) \equiv \boldsymbol{A}$ and $\log(P_{in}) \equiv \boldsymbol{B} \therefore \boldsymbol{\beta} = \frac{A}{B}$ & $\frac{\boldsymbol{\partial\beta}}{\boldsymbol{\beta}} = \sqrt{\left[\left(\frac{\partial A}{A}\right)^2 + \left(\frac{\partial B}{B}\right)^2\right]}$

Now, $\boldsymbol{\partial A} = 0.434\frac{[\partial(P_{out}\lambda_1^3/\alpha)]}{(P_{out}\lambda_1^3/\alpha)} = \frac{0.434}{(P_{out}\lambda_1^3/\alpha)}(P_{out}\lambda_1^3/\alpha) * \sqrt{\left(\frac{\partial P_{out}}{P_{out}}\right)^2 + \left(\frac{3\partial\lambda_1}{\lambda_1}\right)^2}$

$$\therefore \left(\frac{\boldsymbol{\partial A}}{\boldsymbol{A}}\right)^{\mathbf{2}} = \frac{0.188356}{A^2}\left[\left(\frac{\partial P_{out}}{P_{out}}\right)^2 + \left(\frac{3\partial\lambda_1}{\lambda_1}\right)^2\right]$$

$$\text{and } \boldsymbol{\partial B} = 0.434\frac{\partial P_{in}}{P_{in}} \therefore \left(\frac{\boldsymbol{\partial B}}{\boldsymbol{B}}\right)^{\mathbf{2}} = \frac{0.188356}{B^2}\left[\left(\frac{\partial P_{in}}{P_{in}}\right)^2\right]$$

$$\therefore \frac{\boldsymbol{\partial\beta}}{\boldsymbol{\beta}} = \sqrt{\left[\frac{0.188}{A^2}\left[\left(\frac{\partial P_{out}}{P_{out}}\right)^2 + \left(\frac{3\partial\lambda_1}{\lambda_1}\right)^2\right] + \frac{0.188}{B^2}\left[\left(\frac{\partial P_{in}}{P_{in}}\right)^2\right]\right]}$$

$$\& \ \boldsymbol{\partial\beta} = \frac{A}{B}\sqrt{\left[\frac{0.188}{A^2}\left[\left(\frac{\partial P_{out}}{P_{out}}\right)^2 + \left(\frac{3\partial\lambda_1}{\lambda_1}\right)^2\right] + \frac{0.188}{B^2}\left[\left(\frac{\partial P_{in}}{P_{in}}\right)^2\right]\right]} - - - (13)$$

We now substitute in the relevant values in equation (13) to obtain $\boldsymbol{\partial\beta = 0.0129.}$

Hence $\boldsymbol{\beta \pm \partial\beta = 1.9892 \pm 0.0129}$

The theoretical value of β i.e. 2 lies within the limits of experimental uncertainty associated with our experimental readings. Hence, we conclude that our experiment reproduces the theoretical relationship $P_{out} \propto P_{in}^2$ to a reasonable degree.

In addition, we can calculate the maximum power that our set-up should produce based on the quadratic regression curve obtained. From the regression relation $y = 30.166x^{\mathbf{1.9892}}$, where x is the pump power (in W) and y is the SHG output power (in mW), we let x = 10 (maximum pump power) giving y = 2942 mW = 2.94 W. The uncertainty associated with this value computed as follows:

$$y = 30.166x^{\boldsymbol{\beta}}$$

$$\ln y = \ln 30.166 + \beta \ln x \ \therefore \frac{\Delta y}{\Delta\beta}\frac{1}{y} = \ln x$$

$$\Delta y = y \ln x \, \Delta\beta = 87.4 \, mW$$

Hence, we deduce that our set-up should be capable of reaching (2.94 $\pm$ 0.09) W of output power when operating at full capacity.

7.4 Photorefractive Effects

Next, we analyze how the maximum conversion efficiency attainable varies with the crystal temperature. We are trying to investigate if any photorefractive effects (Section 4.5) adversely affect our SHG conversion efficiency at low temperatures. We plot the absolute – instead of normalized – second harmonic power as a function of temperature because the latter would conceal the actual conversion efficiency.

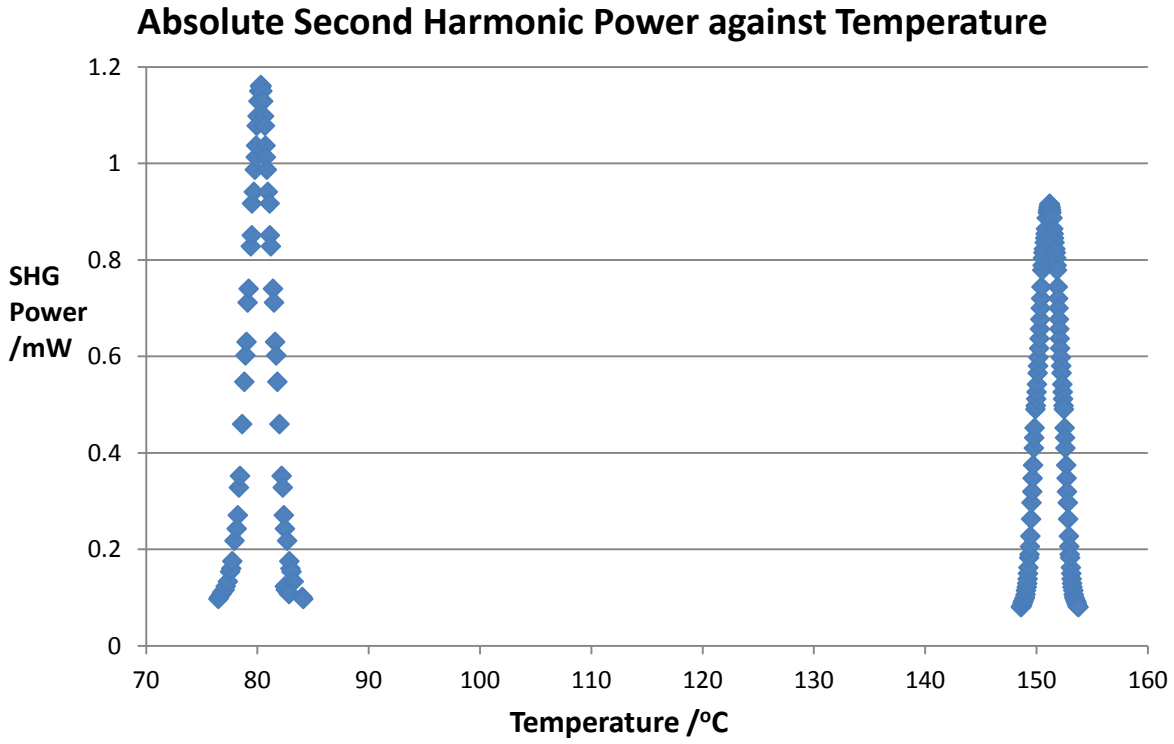

Figure 31: Absolute SHG Power v Temperature to investigate the existence of photorefractive effects in our frequency-doubling process

We observed that, contrary to the discovery of Peil et al [1], we did not achieve any significant enhancement in intensity when the higher temperature was used. The maximum power attainable was in fact lower when the crystal temperature was tuned near 150°C. The logical conclusion is that photorefractive effects are not influencing our crystal.

The most likely reason is that photorefractive effects in nonlinear crystals arise only from prolonged usage of high-intensity laser beams. Our laser amplifier was mostly operated at low powers (~500 mW) to obtain the various graphs in this section, which are independent of the incident power used. Hence, it is possible that photorefractive effects did not even attain a chance to manifest their adverse consequences, allowing us to attain superior conversion efficiency even at relatively low temperatures. It would be interesting to repeat the above readings after subjecting the crystal to a high-powered beam for several months, and then comparing the two graphs to check if there has been any temporal degradation in the conversion efficiency at the lower temperature.

7.5 Temperature Stability of Oven

We look at the temperature stability of the internally-designed oven with respect to time at 80.4 °C.

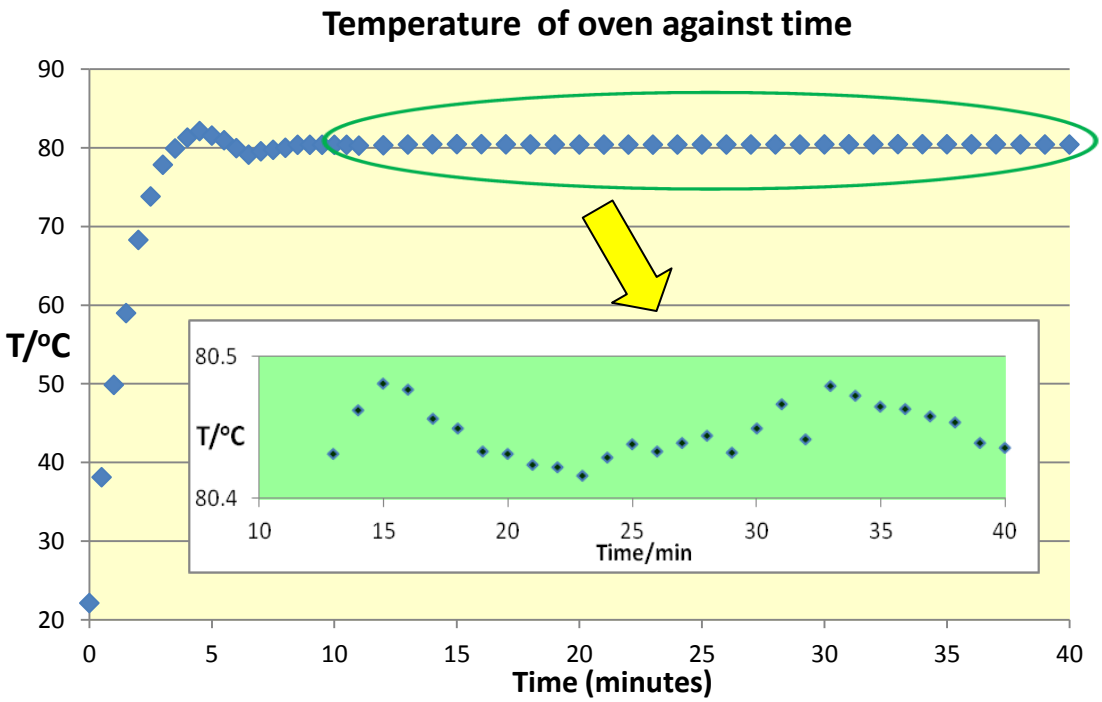

Figure 32: Temperature behavior of the oven used for this paper

The temperature of the oven is highly stable over the duration of usage near 80°C. This is visually evidenced by the temperature profile (beyond eight minutes) having relatively little fluctuations and the

latter, whenever present, were of small magnitude. The longest stretch of continuous observation was about forty minutes, where temperature readings were taken every half-minute for the first ten minutes, and then every minute for the next thirty minutes, for a total of 50 data points, which were then plotted as above. The mean temperature and its standard error were evaluated from a spreadsheet, and are presented hereunder:

$$Temperature\ set\ =\ 80.580\ ^{o}C$$

$$Temperature\ =\ (80.43\ \pm\ 0.04)\ ^{o}C$$

As discussed earlier, a PID regulator (embedded within a Thorlabs Pro 8000 temperature regulator) was used to allow the oven to reach the desired temperature in the shortest possible time, as well as to minimize any random thermal fluctuations by restoring equilibrium within the shortest time interval. These random fluctuations may arise from external events such as lifting the cover of the oven.

Random errors are relatively small ($0.04/80.430 \cong 0.05\%$). Hence, the oven delivers a highly-precise and stable temperature over several minutes of continuous operation, at least. However, the same cannot be said to hold true for systematic errors. At high temperatures, the oven perpetually settled down to a slightly lower temperature than was set. There are two temperatures involved here: the set temperature and the actual measured temperature. The former represents the value input by the user, whereas the latter is the temperature reading obtained by the temperature regulator. The goal is to ensure that the actual measured temperature is as close as possible to the ideal phasematching temperature. We define the difference between the set temperature and the temperature actually obtained as the offset. Near 80.400°C , this value was approximately 0.150°C. Hence, to actually obtain a temperature of 80.430°C, we simply raised the set temperature by the offset (in other words, we set 80.580°C instead of 80.430°C). The offset amount itself (of 0.150°C) was remarkably constant even after multiple cycles of operation. Hence, this persistent offset did not have any material consequence on oven performance.

Initially, we suspected this offset to arise from suboptimal PID values. However, this was ruled out when the offset remained even after thermally equilibrating for several hours. In general, PID values determine the time taken to attain equilibrium, but not the position of the equilibrium itself. Some suboptimal PID values were used to positively confirm this hypothesis.

This paper contends that the offset most likely arises from the fact that the ohmic heating rate can only be changed in discrete steps. The oven works as follows: for each temperature set, there is a heat loss rate as determined by Newton's law of cooling. To maintain thermal equilibrium (or a stable temperature), the resistive heating elements must supply heat at exactly this rate, not higher or lower. However, it is not possible to supply just any value for the power (over a continuous spectrum of values) as the current and voltage values can only change in discrete steps – in increments of 0.001 A and 0.01 V respectively. Consequently, the ohmic heating rate changes in discrete steps as well due to the digital electronics used to measure and supply heating power. Hence, there are certain values for the heat loss rate which the resistors cannot supply exactly. A compromise has to be made and in our case it is apparent that the PID regulator opted for the nearest possible temperature (80.400°C) just below that which was set (83.550°C).

7.6 Stability of Second Harmonic Power

We look at the temporal performance of the second harmonic power obtained. It is important for the SHG set-up to deliver power reliably over extended durations as the success of the subsequent Rubidium spectroscopy (for which this laser is being built) hinges on stable power output levels. Data was taken every 5 seconds, yielding 240 data points over 20 minutes as per Figure 33.

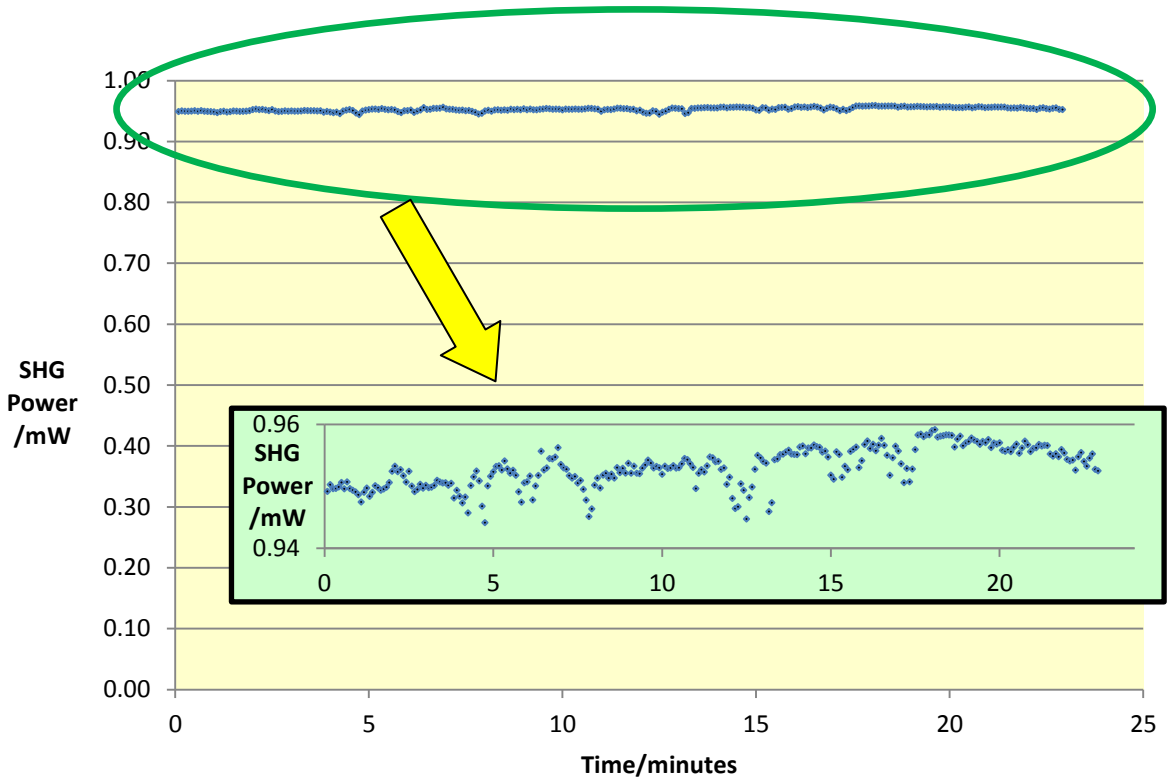

Figure 33: Temporal behavior of the power of the second harmonic output

The mean and standard error are:

$$\text{Power} = (0.953 \pm 0.002)\ \text{mW}$$

The power output is highly stable, and shows relatively minor fluctuations (0.002/0.953 = 0.2%) about a mean value of 0.953 mW. The minute instability is attributable to fluctuations in the oven temperature, the pump wavelength from DFB laser and power levels of fiber amplifier output

7.7 Position of Focal Point

We now look at the effect of varying the position of the focal point within the crystal:

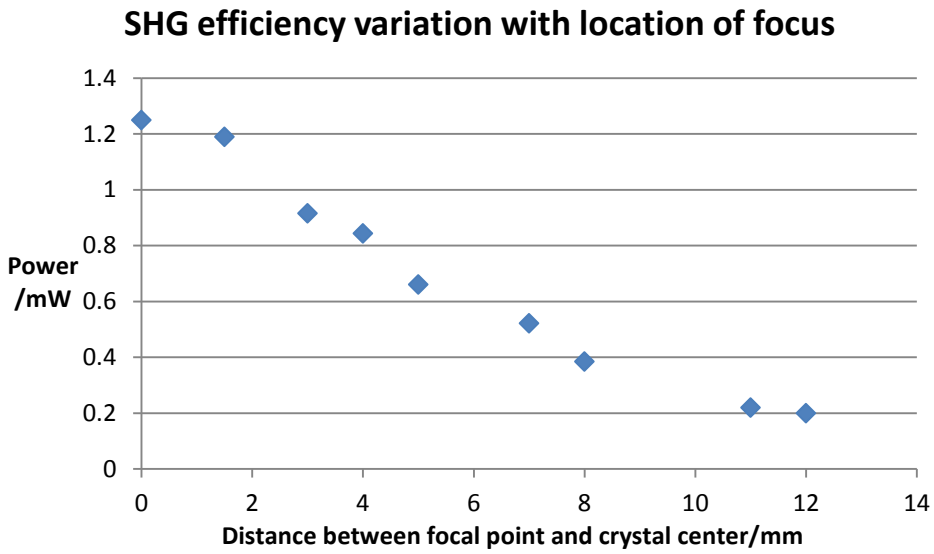

Figure 34: Second harmonic power as a function of the focal point within the crystal

In general, as the focal point of the incident laser beam moves away from the geometrical center of the crystal, the SHG intensity exhibits a marked decline. The data points show considerable fluctuations and do not seem to lend themselves nicely to any curved regression line. This is actually acceptable as there was a large uncertainty in the measurement of distance. The nature of the oven mount allows only one-directional translation along the x-axis with ultra-high precision, whereas the data in this section necessitates moving the oven along the y-axis. A ruler was manually clamped to the optical table and the oven was manually slid along the table. Hence the uncertainty in each distance measurements is about $\pm 0.5mm$. The main purpose of this section is to perform a qualitative analysis to confirm the trend noted by Kleinman and Miller (1966) [14], which it does.

7.8 Stability of Output Wavelength

Lastly, we measure the wavelength of the frequency-doubled beam using a laser wavelength meter. Previously, we looked at the various factors affecting SHG power; however, powers alone are not sufficient if they are not of the correct spectral value, since we have a very precise requirement – rubidium cooling – that needs a 780.240 nm beam. Hence, having the correct wavelength is just as

important as high levels of power. In general, the wavelength is relatively stable about the mean value of 780.24 nm:

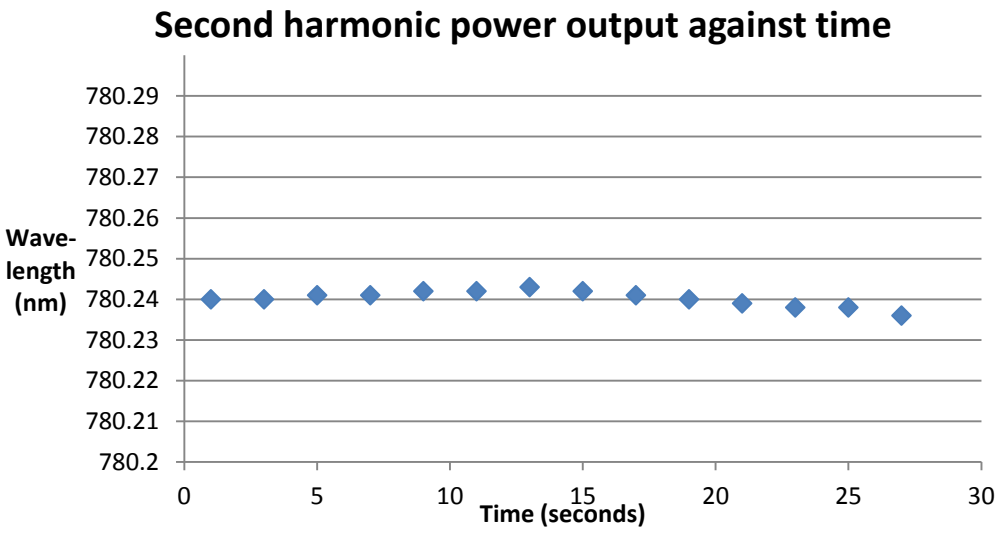

Figure 35: Temporal behavior of the wavelength of the second harmonic output

The mean and standard error are:

$$\text{Wavelength} = (780.240 \pm 0.003)\ \text{nm}$$

Physically, we observed that the wavelength exhibited slow and gradual oscillations about the central value of 780.240 nm. This small instability is marginally attributable to the DFB laser linewidth of 100 kHz. Since $c = f\lambda$, $\frac{\Delta f}{\Delta \lambda} = -\frac{c}{\lambda^2}$ $\therefore \Delta f = -\frac{c}{\lambda^2}\Delta\lambda \; and \; |\Delta f| = \frac{3*10^8}{(780.24*10^{-9})^2} 0.03 * 10^{-9} = 1.48\ GHz.$

Hence the wavelength instability in the second harmonic beam is approximately 0.003 nm, which corresponds to about 1.5 GHz. In truth, 0.003 nm is not the actual linewidth of the emerging beam, so we are using the standard error of the measured output wavelength (which is 0.003 nm) as a guestimate for the true output beam linewidth, which can only be measured directly with an optical spectrum analyser. In any case, our estimated value is several orders of magnitude larger than the 100 kHz linewdith of the seed laser. This is most likely due to frequency drifts of the DFB seed laser.

8 Reliability of data collected

In this sub-section, we discuss some specialized techniques that were employed to improve the reliability of the various figures collected in the previous section. The reliability of the second harmonic power readings depend critically upon how well the harmonic separation was performed. If even a nominal amount of fundamental power (at 1560 nm) leaks into the second harmonic readings (at 780 nm), the second harmonic figures will be grossly inflated. We have taken several steps to eliminate – as far as possible – any chance of having the fundamental laser beam from influencing the second harmonic readings.

Firstly, a double dichroic mirror configuration was used to effect a double filtering of the fundamental 1560 nm beam. Each mirror has a reflectance (dark blue line in Figure 36) of 2.49% at 1560 nm, so a double-configuration would have an effective reflectance of $(2.49\%)^2$ = 0.0622%. This would filter out 99.94% of the incident, unconverted beam.

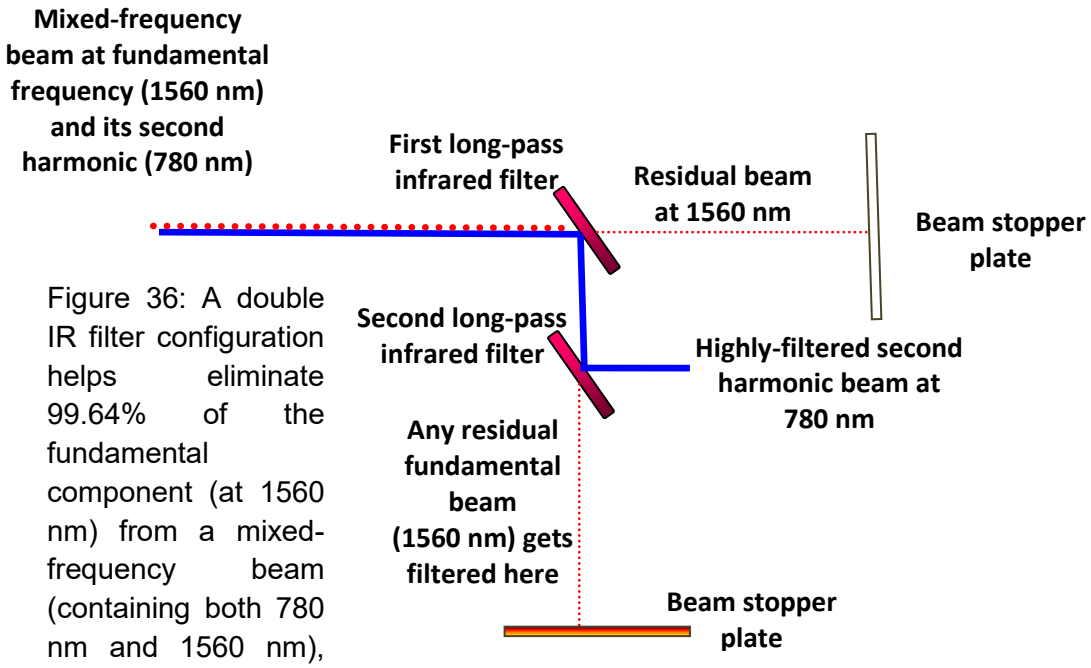

Figure 36: A double IR filter configuration helps eliminate 99.64% of the fundamental component (at 1560 nm) from a mixed-frequency beam (containing both 780 nm and 1560 nm), yielding a pure second harmonic output beam.

Secondly, we used a silicon photodiode with an acceptance window of 400 – 1100 nm. This precludes any chances for the fundamental beam to influence the second harmonic readings, since the detector would not even sense them. This point is only true for the photodiodes we utilized, due to the existence of a cut-off wavelength beyond which the photon energy is below the threshold energy needed to trigger a signal. Using a thermal detector (which measures the total amount of heat detected irrespective of wavelength) would not be able to exploit this property due to the absence of a cut-off wavelength in thermal detectors.

Thirdly, we added a band-pass infrared filter for 780 nm to filter out other light sources that may influence the integrity of our readings.

These are the measures we have implemented to ensure that our second harmonic power readings are accurate and reliable in terms of not being adversely tainted with the fundamental beam.

9 Future research directions

Within time constraints, we have attempted to explore as many aspects of SHG by QPM using a PPLN crystal. Nonetheless, many exciting things remained on the drawing board and we would like to resume work on these areas as soon as possible.

Firstly, we plan to study the wavelength acceptance bandwidth, or the range of wavelengths within which the conversion efficiency is acceptable. The following equation has been obtained by Fejer et al [5]:

$$\Delta\lambda_{\mathbf{HWFM}} = \frac{0.4429\lambda}{L}\left|\frac{n_2 - n_1}{\lambda} + \frac{\partial n_1}{\partial\lambda} + \frac{1}{2}\frac{\partial n_2}{\partial\lambda}\right|^{-1}$$

to describe the SHG power behaviour as the wavelength drifts away from the ideal phasematching value. We would like to generate graphs similar to the temperature bandwidths in Section 7 to study how the experimentally-obtained values compare with those based on theoretical equations.

Secondly, a critical parameter that was left untouched is the confocal parameter. Based upon the Boyd-Kleinman [9] focusing theory, the confocal parameter is an optimizable figure upon which the conversion efficiency of SHG hinges critically. They have discovered that $L/b = 2.84$ (Section 4.2) is the optimal value, but it is worth investigating if that holds true for our set-up since their investigation was based in 1968 on normal birefringent phasematching and not quasi-phase matching. In brief, we would want to test if the switch to quasi-phasematching (wherein there is a finite wavevector mismatch) still maintains the validity of the Boy-Kleinman focusing condition.

We have been unable to determine if any other research group has thus far investigated this value specifically for QPM, so we would be eager to perform it and analyse the results. The main obstacle was the shortage of C-coated lenses of a variety of focal lengths (anti-reflective C-coating implies optimal transmission near 1560 nm, which is crucial to prevent harmful back-reflections into the amplifier). A lens with a particular focal length implies a unique Rayleigh length, since the latter is simply a measure of the curvature about the beam waist. Hence, to perform this investigation, several C-coated lenses of various focal lengths will be needed to investigate the trend between the SHG efficiency and the confocal parameter.

In addition, there are several other interesting things that we could work on, such as using a telecom modulator to generate side bands at the fundamental frequency. In addition, we could place the PPLN crystal in a resonant cavity to check if any resonant cavity enhancement effects improve the SHG efficiency.

10 Safety and Sustainability issues

In this section, we present issues pertaining to high-powered laser causing damage to optical components; we maintain that merely performing an experiment cannot be deemed sufficient until sufficient attention has been paid to the issue of long-term performance and reliability. A short-lived laser is undesirable for its users. A crude way is to ensure that each equipment functions for at least the duration of its standard operating lifetime; an excess signifies success and failure merits introspection. Hereunder, we analyse some of the problems and risks associated with using high-powered lasers.

10.1 Damage threshold of PPLN crystal

It is crucial to avoid optical damage, which may arise from the interaction between the intense laser beam and the lithium niobate crystal. The beam may displace atoms from the lattice to interstitial sites, which would degrade the regular atomic arrangement and, consequently, the optical quality of the crystal. The lifetime of the PPLN should be maximized. The damage threshold of lithium niobate is 100 MW/cm^2 (or 1 MW/mm^2 or 1 TW/m^2) [16].

Looking at Figure 37, a few conclusions can be drawn from it. The chances of optical damage are likely to be greatest at the focus where the spot size is the smallest. Also, on the beam waist, the greatest intensity occurs at the center of the circular beam spot, as dictated by a Gaussian intensity profile. Hence, it suffices to calculate the intensity at the center of the focus. If this value is below the damage threshold, then every other point along the crystal is guaranteed to have even lower intensity. Consequently, the chances of optical damage occurring are remote under normal operating circumstances.

The spot size is measured by a knife-edge technique as depicted in Figure 38, wherein a straight edge knife (for this paper, a piece of silicon with an atomically-flat surface was used) is translated in a parallel fashion from “infinity,” or, more realistically, from several inches away from the laser beam.

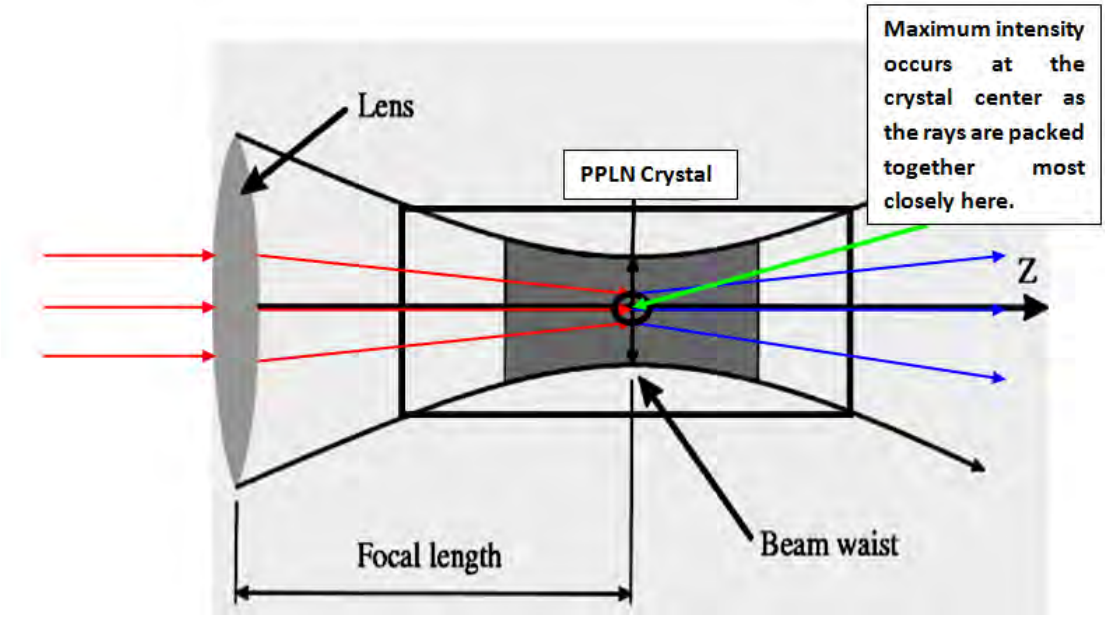

Figure 37: A schematic outline showing that the maximum intensity is expected to occur along the plane with the minimum spot size (known as the beam waist) based on $\text{intensity} = \text{power}/\text{area}$. The entry and exit color of the beam is different, a representation of the frequency-changing process of SHG.

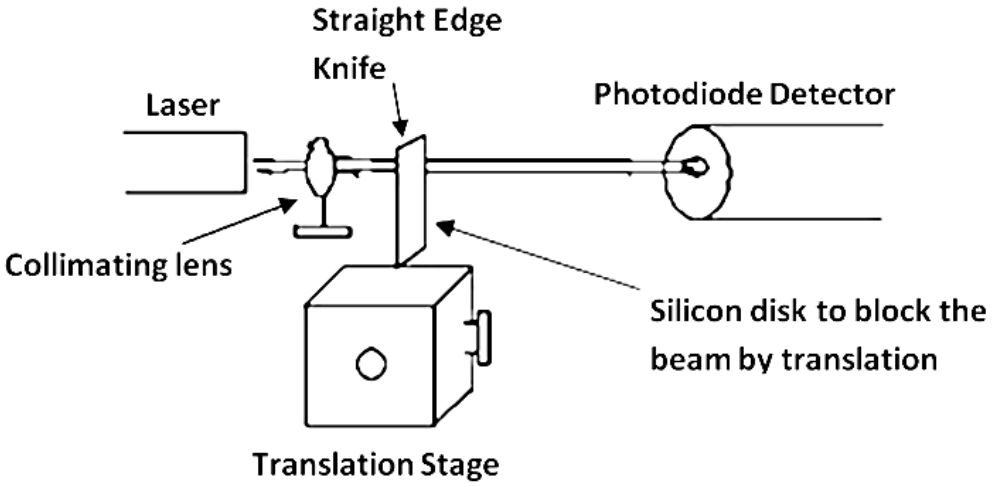

Figure 38: A simplified version of the set-up used to measure the laser spot size.

We measure a modified form of the spot size, known as the 25-75 spot size, as follows. The total power of the beam is measured without any blocking, which is recorded as 2 mW. The beam is then sub-divided into three segments as per Figure 39. The central segment represents 50% of total beam power, and it is flanked by two adjacent segments, each containing 25% of the beam power. The silicon disk is now translated across the beam, until exactly 25% of the beam is clipped, which is practically known when the power meter reading falls from 2 mW to 1.5 mW. This is recorded as x_1. The translation process then resumes till exactly 75% of the beam is clipped, at which point the power meter reads 0.5 mW, which is recorded as x_2. Then, $|x_2 - x_1|$ is defined as the 25-75 spot size.

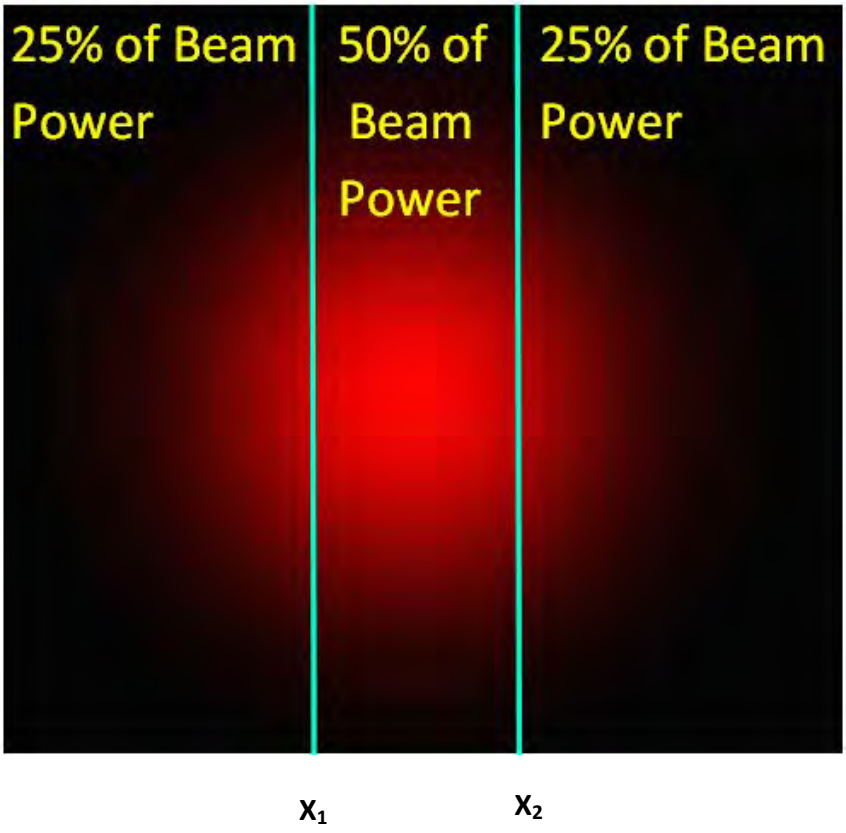

Figure 39: Distribution of total beam power into three convenient segments for measuring the 25-75 spot size.

The measurement procedure in Figure 38 yielded a series of 25-75 spot sizes plotted in Figure 40 and, for reasons outlined in Figure 37, we are only interested in the minimum spot size which, from Figure 40, is 25 μm.

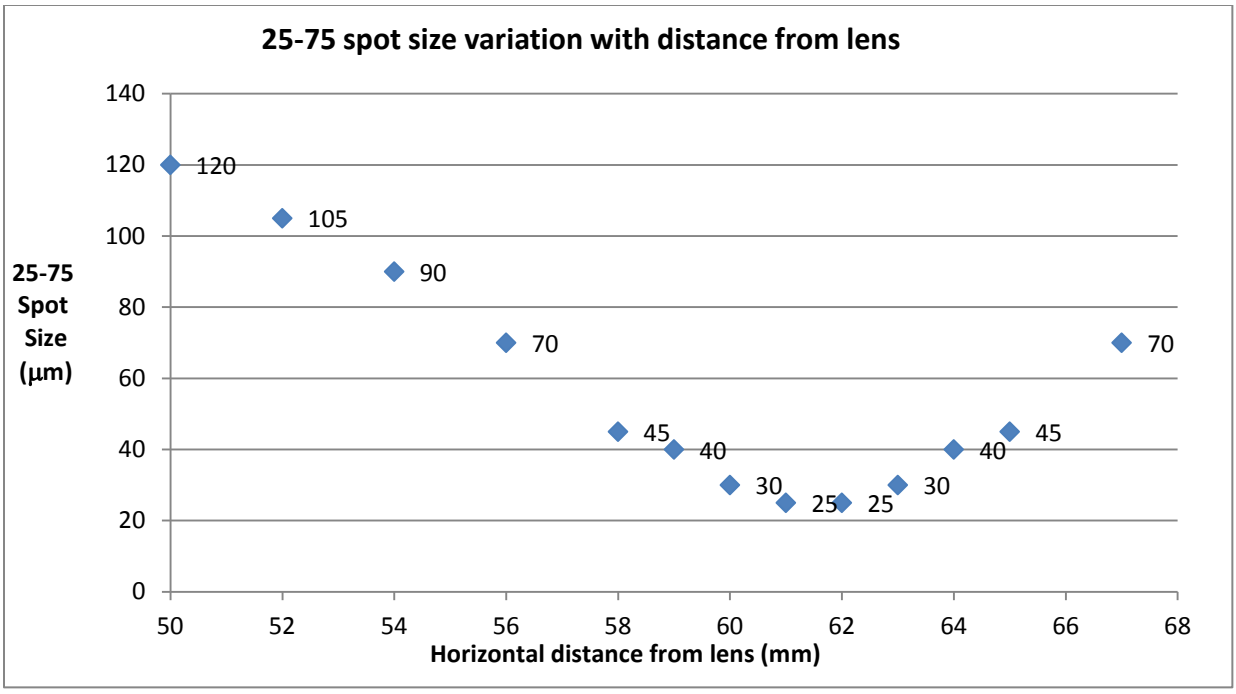

Figure 40: Data representing variation of the 25-75 spot size as a function of distance from the lens. The minimum spot size is simply the lowest point on the curve, which is 25 μm.

Now, the intensity at the center of the beam waist is given as follows:

The Gaussian intensity distribution is

$$I = I_0 e^{-2r^2/w^2}$$

where I_0 is the maximum intensity at the center of the beam (i.e. where r = 0) and w is the $1/e^2$ beam waist radius.

Since

$$I = \frac{dP}{dA},$$

$$\therefore P = \int I\, dA = \int I_0 e^{-2r^2/w^2}\, dA = I_0 \int e^{-2r^2/w^2}\, r\, dr\, d\theta = I_0 \int_0^{2\pi} d\theta \int_0^{\infty} r\, e^{-2r^2/w^2} dr$$

$$= I_0(2\pi) \int_0^{\infty} r\, e^{-\frac{2r^2}{w^2}} dr = I_0(2\pi)\left(\frac{-1}{4/w^2}\right) \int_0^{\infty} -\frac{4r}{w^2} e^{-\frac{2r^2}{w^2}} dr = \frac{w^2 \pi I_0}{2w^2} \int_{\infty}^{0} -\frac{4r}{w^2} e^{-\frac{2r^2}{w^2}}\, dr = \frac{\pi I_0 w^2}{2}$$

$$\therefore I_0 = \frac{2P}{\pi w^2} \text{ where w is the } \frac{1}{e^2} \text{ beam radius.}$$

If we knew w, we could immediately calculate I_0 and be done with. However, the 25-75 spot size measured previously is not the same as the $\frac{1}{e^2}$ beam radius (which is w) in the above formula. Rather, the 25 μm spot size (measured using 25-75 procedure) corresponds to a $1/e^2$ spot size of 30.8 μm (Appendix 2 contains detailed derivation).

$$\therefore I_0 = \frac{2P}{\pi w^2} = \frac{2 * 10\ W}{\pi(15.4\ \mu m)^2} = 2.68 * 10^{10} W/m^2$$

which is below the damage threshold of 10^{12} W/m^2. Hence, under normal operating circumstances, the chances of optical damage occurring to the crystal are remote. It should be mentioned that this intensity of $2.68 * 10^{10} W/m^2$ occurs at a single infinitesimally-small point, and the intensity at other points in the crystal is expected to be much lower, which reinforces the above assertion that the chances of optical damage occurring within the PPLN crystal is remote.

10.2 Laser Induced Damage Threshold

We have just looked at the damage threshold of the PPLN crystal. Now, we turn our attention to the lenses used, since they too could be damaged by the high-powered laser beam. The damage mechanism differs in terms of whether the laser is operated in pulsed or continuous wave (cw) mode.

In pulsed mode, the damage arises from electrons being stripped from the lattice structure of an optic. In cw mode, damage is triggered due to thermal effects arising from heat absorption in the coating or substrate.

Since our laser is operating in cw mode, our focus needs to be on long-term damage arising from thermal absorption by the lenses causing optical degradation. The lenses used for this project had the following stated threshold:

Damage Threshold	5.0 J/cm2 (1542 nm, 10 ns, 10 Hz, Ø0.181 mm)

The laser damage threshold for cw lasers is more dependent on the material and geometric properties of the sample, and therefore, unlike for long-pulse lasers, it is more difficult to specify with a single quantity. This explains why the officially-stated damage threshold is only applicable for pulsed lasers.

A back-of-the-envelope calculation ostensibly indicates that the maximum irradiance allowed prior to the onset of laser-induced lens damage is (5 J/cm^2) /(10 ns) = 500 MW/cm^2 = 5 MW/mm^2. Even though this is the threshold value for pulsed lasers, we can use it as a guestimate for the unknown cw damage threshold. To add a margin of safety since this is only a guestimate, the actual laser intensity used should be much smaller than this pulsed laser damage threshold. Hence, the maximum irradiance on the lens is approximately:

$$\therefore \mathrm{I}_0 = \frac{2\mathrm{P}}{\pi \mathrm{w}^2}\left(\text{where w is the}\frac{1}{\mathrm{e}^2}\text{ beam radius}\right) = \frac{2 * 10\ \mathrm{W}}{\pi(0.55\ \mathrm{mm})^2} = 21\,W/mm^2$$

which is several orders of magnitude lower than the pulsed damage threshold value. Consequently, no conspicuous beam profile degradation was observed over the duration of this experiment, a visible testimony to the fact that the lens did not undergo optical damage over the course of this project.

Note: For this section, the $\frac{1}{\mathrm{e}^2}$ beam radius refers to the beam exiting from the fiber amplifier, which is also the beam striking the lens. The manufacturer's manual gave the $\frac{1}{\mathrm{e}^2}$ beam diameter as 1.1 mm, so the corresponding beam radius is 1.1 mm/2 = 0.55 mm. This simple analysis could not be used in the previous part (section 10.1) as in that case the lens is focusing the beam to a microscopic spot, whose values can only be determined by the measurement procedures outlined in section 10.1. The manufacturer did not specify the post-focusing spot size since this depends on the type of lens used.

Another contentious issue is the use of P = 10 W, whereas our amplifier has a peak rating of 20 W. We return to Figure 15, and observe that the alignment beam needs a PBS cube to be overlapped onto the invisible beam; this PBS cube dumps about half the amplifier output onto a beam-stopper plate, so only half the maximum power actually enters the lens and PPLN crystal. This explains why the maximum power value used in both this and the previous section is 10 W instead of 20 W.

11 Appendix

1. Sellmeier coefficients for MgO-doped Lithium Niobate [8]:

Sellmeier Coefficient	5% MgO:LN
a1	5.756
a2	0.0983
a3	0.2020
a4	189.32
a5	12.52
a6	1.32E-02
b1	2.860E-06
b2	4.700E-08
b3	6.113E-08
b4	1.516E-04

2. Here, we establish a relation between the measured 25-75 spot size and the true $1/e^2$ spot size (to be used for damage threshold calculations). We change from polar to Cartesian coordinates:

$$I = I_0 e^{-\frac{2r^2}{w^2}} = I_0 e^{\frac{-2}{w^2}(x^2+y^2)}$$

$$\therefore P = \int_{x_1}^{\infty}\int_{-\infty}^{\infty} I(x,y)\ dy\,dx = \int_{x_1}^{\infty}\int_{-\infty}^{\infty} e^{-\frac{2(x^2+y^2)}{w^2}}\ dx\,dy = \int_{x_1}^{\infty} e^{-\frac{2x^2}{w^2}}\,dx \int_{-\infty}^{\infty} e^{-\frac{2y^2}{w^2}}\,dy$$

$$\text{Define} \equiv \frac{P(x)}{P(-\infty)} = \frac{\int_{x_1}^{\infty} e^{-\frac{2x^2}{w^2}}\,dx}{\int_{-\infty}^{\infty} e^{-\frac{2x^2}{w^2}}\,dx} = \text{power contained from } x=x_1 \text{ to } x=\infty \text{ over all y.}$$

For a normalized Gaussian distribution, $1 = \frac{1}{\sqrt{2\pi\sigma^2}}\int_{-\infty}^{\infty} e^{-\frac{x^2}{2\sigma^2}}\,dx$

$$\therefore \int_{-\infty}^{\infty} \mathrm{e}^{-\frac{x^2}{2\sigma^2}}\, dx = \sqrt{2\pi}\,\sigma^2 = \sqrt{\pi}\,w^2 \left(\text{after making the substitution } \sigma^2 = \frac{w^2}{4}\right).$$

Hence $\eta = \frac{1}{\sqrt{\pi}\,w^2}\int_{x_1}^{\infty} \mathrm{e}^{-\frac{2x^2}{w^2}}\,\mathrm{dx} = \frac{1}{\sqrt{\pi}\,w^2}\int_{\frac{\sqrt{2}x_1}{w}}^{\infty} \mathrm{e}^{-t^2}\left(\frac{w\,dt}{\sqrt{2}}\right) = \frac{1}{\sqrt{2\pi}w}\int_{\frac{\sqrt{2}x_1}{w}}^{\infty} \mathrm{e}^{-t^2}\,\mathrm{dt} = \frac{1}{\sqrt{2\pi}w}\int_{\frac{\sqrt{2}x_1}{w}}^{\infty} \mathrm{e}^{-t^2}\,\mathrm{dt} =$

$$\frac{2}{\sqrt{8\pi}w}\int_{\frac{\sqrt{2}x_1}{w}}^{\infty} \mathrm{e}^{-t^2}\,\mathrm{dt} = \frac{1}{\sqrt{8}w}\left[\frac{2}{\sqrt{\pi}}\int_{\frac{\sqrt{2}x_1}{w}}^{\infty} \mathrm{e}^{-t^2}\,\mathrm{dt}\right]$$

When $\eta = 0.25 = \frac{1}{\sqrt{8}w}\left[\frac{2}{\sqrt{\pi}}\int_{\frac{\sqrt{2}x_1}{w}}^{\infty} \mathrm{e}^{-t^2}\,\mathrm{dt}\right], \therefore 0.25\sqrt{8}w = \left[\frac{2}{\sqrt{\pi}}\int_{\frac{\sqrt{2}x_1}{w}}^{\infty} \mathrm{e}^{-t^2}\,\mathrm{dt}\right]$

Define $w` = 10^6 w \; and \; let \; x_1 = 12.5\;\mu m, \therefore 0.25\sqrt{8}w = \left[\frac{2}{\sqrt{\pi}}\int_{\frac{\sqrt{2}x_1}{w}}^{\infty} \mathrm{e}^{-t^2}\,\mathrm{dt}\right] = \left[\frac{2}{\sqrt{\pi}}\int_{\frac{17.6}{w`}}^{\infty} \mathrm{e}^{-t^2}\,\mathrm{dt}\right]$

$$\therefore 0.7071w = \left[\frac{2}{\sqrt{\pi}}\int_{\frac{17.6}{w`}}^{\infty} \mathrm{e}^{-t^2}\,\mathrm{dt}\right] = erfc\left(\frac{17.6}{w`}\right)$$

$$\therefore \frac{0.7071w`}{10^6} = erfc\left(\frac{17.6}{w`}\right)$$

Numerical methods give the solution as $w` = 15.4$

$\therefore w = \frac{15.4}{10^6} m = 15.4\;\mu m$

$\therefore \; spot \; size = 2w = 2 * 15.4\;\mu m = 30.8\;\mu m$

12 References

[1] S. Peil, S. Crane, and C. Ekstrom, "High-efficiency frequency doubling for the production of 780 nm light," in Proceedings of the 2003 IEEE International Frequency Control Symposium and PDA Exhibition Jointly with the 17th European Frequency and Time Forum (Tampa, 2003).

[2] Compact Blue-Green Lasers (Cambridge Studies in Modern Optics), W. P. Risk, T. R. Gosnell, A. V. Nurmikko, Cambridge University Press (January 9, 2003)

[3] Introduction to electrodynamics, 3rd Edition, David J. Griffiths, Prentice Hall, 1999

[4] Nonlinear Optics, 2nd Edition, Robert W. Boyd, Academic Press (2003)

[5] M. M. Fejer, G. A. Magel, D. H. Jundt, and R. L. Byer, "Quasi-phase-matched second harmonic generation: tuning and tolerances," IEEE J. Quantum Electron. **28**, 2631–2654 (1992).

[6] Problems and Solutions in Optics & Photonics, A. Ghatak, K. Thyagarajan, Tata McGraw Hill Education (March 17, 2011)

[7] Y. S. Kim and R. T. Smith, "Thermal expansion of lithium tantalate and lithium niobate single crystals," J. Appl. Phys. **40**, 4637–4641 (1969).

[8] O. Gayer, Z. Sacks, E. Galun, and A. Arie, "Temperature and wavelength dependent refractive index equations for MgO-doped congruent and stoichiometric LiNbO3," Appl. Phys.B **91**, 343 (2008).

[9] G. D. Boyd and D. A. Kleinman, "Parametric interaction of focused Gaussian light beams," J. Appl. Phys. **39**, 3596–3639 (1968).

[10] Fundamentals of Photonics, 2nd Edition, Bahaa E. A. Saleh, Malvin Carl Teich, Wiley (February 2007)

[11] Guohui Li, Yanxia Cui, Jing Wang, Photorefractive inhibition of second harmonic generation in periodically poled MgO doped LiNbO3 waveguide, Optics express 21.19 (2013): 21790-21799.

[12] D. Jedrzejczyk, R. Güther, K. Paschke, G. Erbert, and G. Tränkle, "Diode laser frequency doubling in a ppMgO:LN ridge waveguide: influence of structural imperfection, optical absorption and heat generation," Appl.Phys. B **109**(1), 33–42 (2012).

[13] O. A. Louchev, N. E. Yu, S. Kurimura, and K. Kitamura, "Thermal inhibition of high-power second-harmonic generation in periodically poled LiNbO3 and LiTaO3 crystals," Appl. Phys. Lett. **87**(13), 131101 (2005).

[14] Kleinman, D. A., and R. C. Miller. "Dependence of second-harmonic generation on the position of the focus." Physical Review 148.1 (1966): 302.

[15] Sané, S. S., S. Bennetts, J. E. Debs, C. C. N. Kuhn, G. D. McDonald, P. A. Altin, J. D. Close, and N. P. Robins. "11 W narrow linewidth laser source at 780nm for laser cooling and manipulation of Rubidium." Optics express 20, no. 8 (2012): 8915-8919.

[16] Principles of Nonlinear Optics, Guang S He, Song H Liu, World Scientific Pub Co Inc, 1st Edition (February 2000)